Atmos. Chem. Phys. Discuss., 14, 18127–18180, 2014
www.atmos-chem-phys-discuss.net/14/18127/2014/
doi:10.5194/acpd-14-18127-2014

Atmospheric Chemistry and Physics Discussions

Satellite observations of stratospheric carbonyl fluoride

J. J. Harrison[1], M. P. Chipperfield[2], A. Dudhia[3], S. Cai[3], S. Dhomse[2], C. D. Boone[4], and P. F. Bernath[1,5]

[1]Department of Chemistry, University of York, Heslington, York, YO10 5DD, UK
[2]Institute for Climate and Atmospheric Science, School of Earth and Environment, University of Leeds, Leeds, LS2 9JT, UK
[3]Atmospheric, Oceanic and Planetary Physics, Clarendon Laboratory, University of Oxford, Parks Road, Oxford, OX1 3PU, UK
[4]Department of Chemistry, University of Waterloo, 200 University Avenue West, Ontario N2L 3G1, Canada
[5]Department of Chemistry and Biochemistry, Old Dominion University, Norfolk, Virginia 23529, USA

Received: 27 May 2014 – Accepted: 13 June 2014 – Published: 4 July 2014

Correspondence to: J. J. Harrison (jeremy.harrison@york.ac.uk)

Published by Copernicus Publications on behalf of the European Geosciences Union.

Abstract

The vast majority of emissions of fluorine-containing molecules are anthropogenic in nature, e.g. chlorofluorocarbons (CFCs), hydrochlorofluorocarbons (HCFCs), and hydrofluorocarbons (HFCs). These molecules slowly degrade in the atmosphere leading to the formation of HF, COF_2, and COClF, which are the main fluorine-containing species in the stratosphere. Ultimately both COF_2 and COClF further degrade to form HF, an almost permanent reservoir of stratospheric fluorine due to its extreme stability. Carbonyl fluoride (COF_2) is the second most abundant stratospheric "inorganic" fluorine reservoir with main sources being the atmospheric degradation of CFC-12 (CCl_2F_2), HCFC-22 (CHF_2Cl), and CFC-113 ($CF_2ClCFCl_2$).

This work reports the first global distributions of carbonyl fluoride in the Earth's atmosphere using infrared satellite remote-sensing measurements by the Atmospheric Chemistry Experiment Fourier transform spectrometer (ACE-FTS), which has been recording atmospheric spectra since 2004, and the Michelson Interferometer for Passive Atmospheric Sounding (MIPAS) instrument, which has recorded thermal emission atmospheric spectra between 2002 and 2012. The observations reveal a high degree of seasonal and latitudinal variability over the course of a year. These have been compared with the output of SLIMCAT, a state-of-the-art three-dimensional chemical transport model. In general the observations agree well with each other and compare well with SLIMCAT, although MIPAS is biased high by as much as $\sim 30\,\%$.

Between January 2004 and September 2010 COF_2 grew most rapidly at altitudes above ~ 25 km in the southern latitudes and at altitudes below ~ 25 km in the northern latitudes, whereas it declined most rapidly in the tropics. These variations are attributed to changes in stratospheric dynamics over the observation period. The overall COF_2 global trend over this period is calculated as $0.85 \pm 0.34\,\%\,\text{year}^{-1}$ (MIPAS), $0.30 \pm 0.44\,\%\,\text{year}^{-1}$ (ACE), and $0.88\,\%\,\text{year}^{-1}$ (SLIMCAT).

ACPD
14, 18127–18180, 2014

1 Introduction

Although small quantities of fluorine-containing molecules are emitted into the atmosphere from natural sources, e.g. volcanic and hydrothermal emissions (Gribble, 2002), the vast majority of emissions are anthropogenic in nature, e.g. chlorofluorocarbons (CFCs), hydrochlorofluorocarbons (HCFCs), and hydrofluorocarbons (HFCs). Most fluorine in the troposphere is present in its emitted "organic" form due to these molecules having typical lifetimes of a decade or longer, however photolysis in the stratosphere, which liberates fluorine atoms that react with methane, water or molecular hydrogen, result in the formation of the "inorganic" product hydrogen fluoride, HF. At the top of the stratosphere ($\sim$ 50 km altitude), $\sim$ 75 % of the total available fluorine is present as HF (Brown et al., 2014). Due to its extreme stability, HF is an almost permanent reservoir of stratospheric fluorine, meaning the atmospheric concentrations of F and FO, necessary for an ozone-destroying catalytic cycle, are very small (Tressaud, 2006). For this reason fluorine does not cause any significant ozone loss. HF is removed from the stratosphere by slow transport to, and rainout in, the troposphere, or by upward transport to the mesosphere, where it is destroyed by photolysis (Duchatelet et al., 2010). The recent stratospheric fluorine inventory for 2004–2009 (Brown et al., 2014) indicates a year-on-year increase of HF and total fluorine.

The second most abundant stratospheric "inorganic" fluorine reservoir is carbonyl fluoride (COF_2), largely due to its slow photolysis. Recent studies indicate that its atmospheric abundance is increasing (Duchatelet et al., 2009; Brown et al., 2011). The main sources of COF_2 are the atmospheric degradation of CFC-12 (CCl_2F_2) and CFC-113 ($CF_2ClCFCl_2$), which are both now banned under the Montreal Protocol, and HCFC-22 (CHF_2Cl), the most abundant HCFC and classed as a transitional substitute under the Montreal Protocol. Although the amounts of CFC-12 and CFC-113 in the atmosphere are now slowly decreasing, HCFC-22 is still on the increase. For the two most abundant source molecules, CFC-12 and HCFC-22, the atmospheric degradation proceeds

ACPD
14, 18127–18180, 2014

by their initial breakdown into CF_2Cl (Tressaud, 2006),

$$CF_2Cl_2 + h\nu \rightarrow CF_2Cl + Cl$$
$$CHF_2Cl + OH \rightarrow CF_2Cl + H_2O \quad \text{(R1)}$$

followed by

$$CF_2Cl + O_2 + M \rightarrow CF_2ClO_2 + M$$
$$CF_2ClO_2 + NO \rightarrow CF_2ClO + NO_2$$
$$CF_2ClO + O_2 \rightarrow COF_2 + ClO_2. \quad \text{(R2)}$$

For CFC-113 and more minor sources such as HFCs (e.g. HFC-134a, HFC-152a), the reaction scheme is similar.

COF_2 volume mixing ratios (VMRs) slowly increase with altitude up to the middle of the stratosphere, above which they decrease as photolysis of COF_2 becomes more efficient, leading to the formation of fluorine atoms,

$$COF_2 + h\nu \rightarrow FCO + F$$
$$FCO + O_2 + M \rightarrow FC(O)O_2 + M$$
$$FC(O)O_2 + NO \rightarrow FCO_2 + NO_2$$
$$FCO_2 + h\nu \rightarrow F + CO_2. \quad \text{(R3)}$$

As mentioned earlier, these F atoms react with CH_4, H_2O or H_2 to form HF.

Vertical profiles of COF_2 in the atmosphere have previously been determined from measurements taken by the Atmospheric Trace MOlecule Spectrometry Experiment (ATMOS) instrument which flew four times on NASA space shuttles between 1985 and 1994 (Rinsland et al., 1986; Zander et al., 1994). Additionally, there have been several studies into the seasonal variability of COF_2 columns above Jungfraujoch using ground-based Fourier transform infrared (FTIR) solar observations (Mélen et al., 1998; Duchatelet et al., 2009).

The use of satellite remote-sensing techniques allows the measurement of COF_2 atmospheric abundances with global coverage, and the investigation more fully of COF_2

ACPD
14, 18127–18180, 2014

trends, and seasonal and latitudinal variability. This work presents the first global distributions of COF_2 using data from two satellite limb instruments: the Atmospheric Chemistry Experiment Fourier transform spectrometer (ACE-FTS), onboard the SCISAT satellite, which has been recording atmospheric spectra since 2004, and the Michelson Interferometer for Passive Atmospheric Sounding (MIPAS) instrument (Fischer et al., 2008) onboard the ENVIronmental SATellite (Envisat), which has recorded thermal emission atmospheric spectra between 2002 and 2012. The observations are compared with the output of SLIMCAT, a state-of-the-art three-dimensional (3-D) chemical transport model (CTM). Trends in COF_2 VMRs between 2004 and 2010 are calculated and discussed.

2 Retrieval of carbonyl fluoride

2.1 ACE-FTS spectra

The ACE-FTS instrument, which covers the spectral region 750 to 4400 cm^{-1} with a maximum optical path difference (MOPD) of 25 cm and a resolution of 0.02 cm^{-1} (using the definition of 0.5/MOPD throughout), uses the sun as a source of infrared radiation to record limb transmission through the Earth's atmosphere during sunrise and sunset ("solar occultation"). Transmittance spectra are obtained by ratioing against exo-atmospheric "high sun" spectra measured each orbit. These spectra, with high signal-to-noise ratios, are recorded through long atmospheric limb paths ($\sim$ 300 km effective length), thus providing a low detection threshold for trace species. ACE has an excellent vertical resolution of about 3–4 km and can measure up to 30 occultations per day, with each occultation sampling the atmosphere from 150 km down to the cloud tops (or 5 km in the absence of clouds). The locations of ACE occultations are dictated by the low Earth circular orbit of the SCISAT satellite and the relative position of the sun. Over the course of a year, the ACE-FTS records atmospheric spectra over a large portion of the globe (Bernath et al., 2005).

ACPD
14, 18127–18180, 2014

The atmospheric pressure and temperature profiles, the tangent heights of the measurements, and the carbonyl fluoride VMRs were taken from the version 3.0 processing of the ACE-FTS data (Boone et al., 2005, 2013). Vertical profiles of trace gases (along with temperature and pressure) are derived from the recorded transmittance spectra via an iterative Levenberg–Marquardt nonlinear least-squares global fit to the selected spectral region(s) for all measurements within the altitude range of interest, according to the equation

$$\boldsymbol{x}_{i+1} = \boldsymbol{x}_i + \left(\mathbf{K}^{\mathrm{T}}\mathbf{S}_y^{-1}\mathbf{K} + \lambda\mathbf{I}\right)^{-1}\mathbf{K}^{\mathrm{T}}\mathbf{S}_y^{-1}\left(\boldsymbol{y} - \mathbf{F}\left(\boldsymbol{x}_i, \boldsymbol{b}\right)\right). \quad (1)$$

In Eq. (1), $\boldsymbol{x}$ is the state vector, i.e. the atmospheric quantities to be retrieved, $\boldsymbol{y}$ the vector of measurements (over a range of tangent heights), $\mathbf{S}_y$ the measurement error covariance matrix (assumed to be diagonal), λ the Levenberg–Marquardt weighting factor, $\mathbf{F}$ the radiative transfer (forward) model, $\boldsymbol{b}$ the forward model parameter vector, i the iteration number, and $\mathbf{K}$ is the Jacobian matrix ($\equiv \partial\mathbf{F}/\partial\boldsymbol{x}$).

The microwindow set and associated altitude ranges are listed in Table 1. The VMRs for molecules with absorption features in the microwindow set (see Table 2) were adjusted simultaneously with the COF_2 amount. All spectroscopic line parameters were taken from the HITRAN 2004 database (Rothman et al., 2005). The v3.0 COF_2 retrieval extends from a lower altitude of 12 km up to 34 km at the poles and 45 km at the equator, with the upper limit varying with latitude (see Table 1). For ACE spectra recorded at tangent heights that fall within the selected retrieval altitude range, the initial VMRs (which do not vary with season or latitude) for the least-squares fit are taken from the set of VMR profiles established by the ATMOS mission (Irion et al., 2002). The COF_2 spectral signal in ACE spectra recorded above the upper altitude retrieval limit (see Table 1) is generally below the noise level, making it impossible to directly retrieve VMRs at these altitudes. However, the ATMOS profile indicates that the COF_2 VMRs do not effectively drop to zero until ∼ 55 km. To compensate, the portion of the retrieved VMR profile above the highest analysed ACE measurement is calculated by scaling this AT-

ACPD
14, 18127–18180, 2014

MOS, or a priori, profile in that altitude region; this scaling factor is determined during the least-squares fitting.

An ACE-FTS transmittance spectrum in the region of one of the microwindows is plotted in the top panel of Fig. 1. This measurement comes from occultation ss11613 (recorded on 9 October 2005 south of Mexico, over the Pacific Ocean) at a tangent height of 28.9 km. The second panel reveals the calculated contribution to the measurement of COF_2 based on its retrieved VMR (~ 3 %); three spectral features are clearly due to absorption of COF_2. The third panel gives the observed – calculated residuals for the retrieval without the inclusion of COF_2 in the forward model; the shape of these residuals matches well with the calculated COF_2 contribution. The bottom panel contains the observed – calculated residuals, indicating the goodness of the fit.

2.2 MIPAS spectra

The MIPAS instrument, a Fourier transform spectrometer, measures the thermal limb emission of the Earth's atmosphere in the mid-infrared spectral region, 685–2410 cm^{-1}. Launched in March 2002, the first two years of spectra were recorded at an unapodised resolution of 0.025 cm^{-1} (MOPD = 20 cm). The nominal scan pattern consisted of 17 tangent points per scan (FR17, FR = full resolution) from 6–68 km altitude with a minimum vertical spacing of 3 km. A mechanical degradation of the interferometer's mirror drive led to a cessation in measurements, with a resumption in operations in January 2005 at a reduced resolution of 0.0625 cm^{-1} (MOPD = 8 cm). The new nominal scan pattern consisted of 27 tangent points per scan (OR27, OR = optimised resolution) over altitude ranges that varied with latitude, from 5–70 km at the poles to 12–77 km at the equator; this variation, which approximately follows the tropopause shape, minimises the number of spectra lost to cloud contamination. The vertical spacing of OR27 scans ranges from 1.5 km at lower altitudes and 4.5 at higher altitudes. Note that the reduction in scan time associated with the lower spectral resolution resulted in an increase in the number of tangent points (an additional ten) within the limb scan,

ACPD
14, 18127–18180, 2014

thus improving the vertical resolution. MIPAS data are available until April 2012, when communication with the ENVISAT satellite failed.

Retrievals were performed using v1.3 of the Oxford L2 retrieval algorithm MORSE (MIPAS Orbital Retrieval using Sequential Estimation; http://www.atm.ox.ac.uk/MORSE/) with ESA v5 L1B radiance spectra. The equivalent to Eq. (1) in an optimal estimation approach is (e.g. Rodgers, 2000):

$$\boldsymbol{x}_{i+1} = \boldsymbol{x}_i + \left[(1+\lambda)\mathbf{S}_\mathrm{a}^{-1} + \mathbf{K}_i^\mathrm{T}\mathbf{S}_y^{-1}\mathbf{K}_i^\mathrm{T}\right]^{-1}\left\{\mathbf{K}_i^\mathrm{T}\mathbf{S}_y^{-1}\left[\boldsymbol{y} - \mathbf{F}(\boldsymbol{x}_i, \boldsymbol{b})\right] - \mathbf{S}_\mathrm{a}^{-1}\left[\boldsymbol{x}_i - \boldsymbol{x}_\mathrm{a}\right]\right\}, \quad (2)$$

where the new terms $\boldsymbol{x}_\mathrm{a}$ and $\mathbf{S}_\mathrm{a}$ represent the a priori estimate of $\boldsymbol{x}$ and its error covariance, respectively. However, rather than applying the above equation to the full set of measurements $\boldsymbol{y}$, MORSE uses a sequential estimation approach (Rodgers, 2000) and applies Eq. (2) successively to spectral subsets defined by each microwindow at each tangent altitude. For this work, the a priori estimate is taken from IG2 COF_2 profiles (Remedios et al., 2007). The spectral microwindows and associated altitude ranges are listed in Table 3; the retrieval extends from a lower altitude of 7.5 up to 54.0 km. For COF_2 retrievals, the MORSE state vector consists of the profile of COF_2 plus, for each microwindow (see Table 4), a profile of atmospheric continuum and a radiometric offset (intended to remove any spectrally smooth background variations within each microwindow, e.g., due to aerosols or thin clouds as well as any residual altitude-dependent radiometric offsets). The forward model uses pressure, temperature and the abundances of major contaminating species (H_2O, O_3, HNO_3, CH_4, N_2O and NO_2) retrieved earlier from the same spectra (using MORSE), and IG2 profiles for other minor gases. Spectroscopic data were taken from the MIPAS PF3.2 database (Flaud et al., 2006), with the COF_2 data in this compilation coming from the HITRAN 2004 database (Rothman et al., 2005). As with all MORSE VMR retrievals, the diagonal elements of $\mathbf{S}_\mathrm{a}$ were set to $(100\,\%)^2$; since MORSE retrieves ln(VMR) rather than VMR, the $\mathbf{S}_\mathrm{a}$ diagonal elements are profile-independent. The off-diagonal elements of $\mathbf{S}_\mathrm{a}$ are set assuming a (strong) vertical correlation length of 50 km, which provides regularisation at

ACPD
14, 18127–18180, 2014

the expense of vertical resolution. Finally, cloud-contaminated spectra were removed using the cloud index method (Spang et al., 2004) with a threshold value of 1.8.

Note that unlike the ACE-FTS retrievals, MORSE retrieves COF_2 at altitudes well above the VMR maximum, even though the information at high altitude is almost entirely from the a priori profiles. Thus, any special treatment to scale the a priori is not required, although, through the vertical correlation, the effect is similar to that explicitly applied for ACE. Additionally, unlike ACE, MORSE uses MIPAS spectra with the Norton Beer strong apodisation applied, hence $\mathbf{S}_y$ is banded rather than diagonal.

Figure 2 provides a plot that illustrates the COF_2 spectral feature in one of the MIPAS microwindows. The top panel shows an averaged MIPAS radiance spectrum (in black) interpolated to 20 km altitude from equatorial measurements taken in March 2010 for the 772–775 cm^{-1} microwindow; in red is the averaged calculated spectrum based on the averaged retrieved VMRs, but without the inclusion of COF_2 in the forward model. The second panel reveals the averaged calculated COF_2 contribution to the spectrum. The third panel gives the observed – calculated residuals for the retrieval (in black), again without the calculated COF_2 contribution; the shape of these residuals matches well with the calculated COF_2 contribution in the second panel. Overlaid in red are the overall observed – calculated residuals, indicating the goodness of the retrieval.

Note that for comparison with ACE-FTS v3.0 COF_2 VMR profiles, the COF_2 MIPAS profiles are interpolated from the standard pressure grid onto the same 1 km grid used by ACE.

3 Retrieval errors

3.1 Infrared spectroscopy of carbonyl fluoride

Retrieving COF_2 VMR profiles from ACE-FTS and MIPAS spectra crucially requires accurate laboratory COF_2 spectroscopic measurements. Uncertainty in the laboratory data can directly contribute to systematic errors in the COF_2 retrievals. The retrievals

ACPD
14, 18127–18180, 2014

reported here make use of three band systems of COF_2; these bands largely correspond to the ν_1 (1943 cm^{-1}; CO stretch), ν_4 (1243 cm^{-1}; CF_2 antisymmetrical stretch), and ν_6 (774 cm^{-1}; out-of-plane deformation) fundamental modes.

Both ACE-FTS and MIPAS retrievals make use of the COF_2 linelist first released as part of the HITRAN 2004 database (and remaining unchanged for the HITRAN 2008 release), with partition data taken from the TIPS subroutine included in the HITRAN compilation. In particular, the ACE-FTS retrieval makes use of spectroscopic lines in the ν_1 and ν_4 bands, whereas MIPAS uses ν_4 and ν_6.

HITRAN employs error codes in the form of wavenumber errors for the parameters ν (line wavenumber) and δ_{air} (air pressure-induced line shift) and percentage errors for S (line intensity), γ_{air} (air-broadened half-width), γ_{self} (self-broadened half-width), and n_{air} (temperature-dependence exponent for γ_{air}). Each error code corresponds to an uncertainty range, but with no information as to how the parameters are correlated.

In HITRAN the parameter δ_{air} (air pressure-induced line shift) is assumed to have a value of 0 $cm^{-1}\,atm^{-1}$. The same values of γ_{air} (0.0845 $cm^{-1}\,atm^{-1}$ at 296 K), γ_{self} (0.175 $cm^{-1}\,atm^{-1}$ at 296 K), and n_{air} (0.94) are used for all COF_2 spectral lines in HITRAN; according to the error codes these values are averages/estimates. They are taken from the work of May (1992), who determined these average parameters for selected lines in the ν_4 and ν_6 bands from measurements made by a tunable diode-laser spectrometer. For the ν_1 band most of the spectral lines used in the retrievals have stated intensity uncertainties $\geq$ 20 %, for the ν_4 band between 10 % and 20 %, and for the ν_6 band the errors are listed as unreported/unavailable. After performing the MIPAS retrievals, the latest HITRAN2012 update was released, which revises the ν_6 band and includes several weak hot bands. The listed intensity uncertainties for this band have been revised to between 10 % and 20 %; spectral simulations indicate only minor intensity differences in the ν_6 band Q branch between the two linelists.

As part of the present study, a comparison was made between an N_2-broadened (760 Torr) composite spectrum of COF_2 (determined from multiple pathlength–concentration burdens) at 278 K and 0.112 cm^{-1} resolution, taken from the Pacific

ACPD
14, 18127–18180, 2014

Northwest National Laboratory (PNNL) IR database (Sharpe et al., 2004) with a synthetic spectrum calculated using HITRAN2004 COF_2 line parameters for the same experimental conditions; the maximum systematic error of the PNNL intensities is 2.5 % (1σ). The comparison reveals that the integrated ν_1 and ν_4 band intensities in the PNNL spectrum are ∼ 15 % higher than HITRAN, whereas the integrated intensity of the very strong Q branch in the ν_6 band of the PNNL spectrum is ∼ 20–25 % higher than HITRAN. Furthermore, the air-broadened half-width in HITRAN for this Q branch appears to be too large at 760 Torr. May (1992) states that the average pressure-broadening coefficients, which are included in HITRAN, could not reproduce the experimental pressure-broadened spectra satisfactorily over the full Q-branch region. The author suggests this may be a result of the J (rotational quantum number)-dependence of the pressure-broadening coefficients or other effects such as line mixing (Hartmann et al., 2008).

When selecting appropriate ACE microwindows from the ν_1 and ν_4 bands, it was noticed that a number of COF_2 lines suffered from systematic bad residuals. Since the COF_2 lines occur in clusters, i.e. are not isolated, there is a strong suggestion that line mixing is playing a role; unfortunately there are no available spectroscopic line parameters that describe line mixing for COF_2. Although the ACE v3.0 retrieval only employs lines with the best residuals, there could still remain a small contribution to the error from the neglect of line mixing. On the other hand, lines in the ν_6 Q branch (employed in the MIPAS retrievals) are very tightly packed, so if line mixing effects are important, errors arising from their neglect will likely be larger for MIPAS retrievals compared with ACE. Unfortunately it is an almost impossible task to quantify these errors without accurate quantitative measurements at low temperatures and pressures. For the purposes of this work it is estimated that retrieval errors arising from COF_2 spectroscopy are at most ∼ 15 %, however since different bands are used in the respective retrievals, it is likely there will be a relative spectroscopic-induced bias between the two schemes.

ACPD
14, 18127–18180, 2014

3.2 ACE-FTS spectra

The ACE v2.2 COF_2 data product has previously been validated against measurements taken by the JPL MkIV interferometer, a balloon-borne solar occultation FTS (Velazco et al., 2011). Unlike the v3.0 product, the upper altitude limit for the v2.2 retrieval is fixed at 32 km, with the scaled ACE a priori profile used above 32 km. MkIV and ACE v2.2 profiles from 2004 and 2005 agree well within measurements error. However, it must be recognised that both retrievals make use of the same COF_2 spectroscopic data, which has an estimated systematic error of at most ∼ 15 % (see Sect. 3.1).

For a single ACE profile, the 1σ statistical fitting errors are typically ∼ 10–30 % over most of the altitude range. These errors are random in nature and are largely determined by the measured signal-to-noise ratios of the ACE-FTS spectra, i.e. measurement noise. For averaged profiles, the random errors are small (reduced by a factor of $1/\sqrt{N}$, where N is the number of profiles averaged) and the systematic errors dominate.

Spectroscopic sources of systematic error predominantly arise from the COF_2 HITRAN linelist (∼ 15 %; see Sect. 3.1), with minor contributions from interfering species that absorb in the microwindow regions. Since the baselines of the ACE-FTS transmittance spectra and the VMRs of the interferers (H_2O, CO_2, O_3, N_2O, CH_4, NO_2, NH_3, HNO_3, HOCl, HCN, H_2O_2, CCl_4, $ClONO_2$, N_2O_5) are fitted simultaneously with the COF_2 VMR, it is not a trivial exercise to determine how much they contribute to the overall systematic error of the COF_2 retrieval. In this work, the view is taken that the lack of systematic features in the spectral residuals indicates that these contributions are small, at most 1 %.

In addition to spectroscopic errors, uncertainties in temperature, pressure, tangent altitude (i.e. pointing) and instrumental line shape (ILS) all contribute to systematic errors in the retrieved COF_2 profiles. To estimate the overall systematic error, the retrieval was performed for small subsets of occultations by perturbing each of these quantities (b_j) in turn by its assumed 1σ uncertainty ($\Delta\, b_j$), while keeping the others unchanged.

ACPD
14, 18127–18180, 2014

The fractional retrieval error, μ_j, is defined as

$$\mu_j = \left| \frac{\mathrm{VMR}(b_j + \Delta b_j) - \mathrm{VMR}(b_j)}{\mathrm{VMR}(b_j)} \right|. \quad (3)$$

Note that for the ACE-FTS retrievals, pressure, temperature and tangent height are not strictly independent quantities; tangent heights are determined from hydrostatic equilibrium, and so these quantities are strongly correlated. For the purposes of this work, only two of these quantities are altered: temperature is adjusted by 2 K and tangent height by 150 m (Harrison and Bernath, 2013). Additionally, ILS uncertainty is induced by adjusting the field of view by 5 % (Harrison and Bernath, 2013). A small subset of occultations was selected for this analysis. The fractional value estimates of the systematic uncertainties, and their symbols, are given in Table 6. Assuming these quantities are uncorrelated, the overall systematic error in the COF_2 retrieval can be calculated as

$$\mu^2_{\mathrm{systematic}} = \mu^2_{\mathrm{spec}} + \mu^2_{\mathrm{int}} + \mu^2_T + \mu^2_z + \mu^2_{\mathrm{ILS}}. \quad (4)$$

The total systematic error contribution to the ACE-FTS COF_2 retrieval is estimated to be ~ 16 %.

As discussed in Sect. 3.1, the COF_2 absorption signal in ACE-FTS spectra decreases relative to the noise as the retrieval extends to higher altitude despite the a priori profile indicating that the COF_2 VMRs do not effectively drop to zero until ~ 55 km. For this reason an upper altitude limit (see Table 1) is set; the retrieval is pushed as high in altitude as possible. The portion of the retrieved VMR profile above the highest analysed ACE measurement (i.e. the spectrum at the highest tangent height, just below the upper altitude limit) is calculated by scaling the a priori profile.

In an ACE retrieval, the calculated spectrum is generated from the sum of contributions from the tangent layer up to 150 km. For the highest analysed measurement, the retrieved VMR in the tangent layer is generated from the piecewise quadratic interpolation scheme (Boone et al., 2005, 2013), while the VMR in every layer above that will

ACPD
14, 18127–18180, 2014

come from scaling the a priori profile; the scaling factor largely comes from forcing the calculated spectrum to match as best as possible the measured spectrum for this one measurement. If the shape of the a priori profile above the highest analysed measurement is incorrect, the contribution to the calculated spectrum from that altitude region will be incorrect for the second highest measurement analysed; the VMRs between the tangent layers of the two highest analysed measurements are adjusted in the retrieval to compensate. Therefore, errors in the a priori VMR profile will introduce systematic errors into the highest altitudes of the retrieved profile.

3.3 MIPAS spectra

The precision, or random error, of the retrieved COF_2 VMRs is calculated via the propagation of the instrument noise and the a priori error through the standard optimal estimation retrieval (using the MORSE code). The total retrieval covariance matrix (neglecting systematic errors) is given by (Rodgers, 2000),

$$\hat{\mathbf{S}} = \mathbf{S}_a - \mathbf{S}_a\mathbf{K}^T\left(\mathbf{K}\mathbf{S}_a\mathbf{K}^T + \mathbf{S}_y\right)^{-1}\mathbf{K}\mathbf{S}_a. \quad (5)$$

Note that this expression effectively represents a combination of the noise-induced random error and the assumed a priori error covariance (sometimes called "smoothing error"), and that some caution is required if interpolating error profiles to different grids. Profile levels with random errors larger than 70 %, mostly at the top and bottom of the retrieval range, are discarded from the dataset and not used in the analysis. Since the a priori profiles have an assumed error of 100 %, this ensures that the retrieved profile levels contain, at worst, ~ 50 % contribution from the a priori. For a single profile, the noise error is typically 5–15 % between 20–40 km, covering the peak of the COF_2 VMR profile; over this range the contribution to the retrieved profiles principally comes from the measurements. Outside this range, the errors increase rapidly as the COF_2 VMR decreases, and the contribution to the retrieved profiles from the a priori increases.

ACPD
14, 18127–18180, 2014

The total error is computed by propagating a number of independent error sources expressed as spectra through the retrieval gain matrix, including both spectral correlations and correlations through the pressure-temperature retrieval. For a single profile, the primary error sources are the measurement noise followed by assumed uncertainties in the O_3 (stratosphere) and N_2O (troposphere) concentrations, which typically contribute 15 % uncertainty in retrieved COF_2 values. Spectroscopic errors in interfering molecules are treated as a single error, assuming a position uncertainty of 0.001 cm^{-1}, 5 % in line strength and 0.1 cm^{-1} in the half-width of COF_2 lines. Figure 3 shows the single-profile error budget for COF_2, with total errors typically 20–30 % between 20–40 km.

MIPAS COF_2 profiles are retrieved at the tangent points of each measurement; these vary from scan to scan. The conversion to absolute altitude for comparison with ACE-FTS COF_2 profiles relies on the MIPAS pointing information, which may lead to a vertical offset of a few hundred metres relative to ACE.

The quality of the MIPAS COF_2 retrieval can be measured using the averaging kernel matrix (Rodgers, 2000), **A**,

$$\mathbf{A} = \mathbf{S}_a\mathbf{K}^T\left(\mathbf{K}\mathbf{S}_a\mathbf{K}^T + \mathbf{S}_y\right)^{-1}\mathbf{K} = \mathbf{I} - \hat{\mathbf{S}}\mathbf{S}_a^{-1}, \quad (6)$$

where **I** is the identity matrix. In general, for a given profile, rows of **A** are peaked functions, peaking at the appropriate altitude range for the observation; the width of each function is a measure of the vertical resolution of each COF_2 observation.

Figures 4–6 contain plots of averaging kernels for three profiles taken during 22 March 2011 (Spring Equinox) at 80° S, 0° and 80° N latitude, respectively. In each figure, the top left panel shows the retrieved profile (with random error bars), its associated a priori profile, and the median of all the profiles that day within 5° latitude. The top right panel shows the corresponding random error to the profile; in each case ~ 10 % at the profile peak. The bottom left plot gives the averaging kernel rows, with crosses on the right axis marking the perturbation height for each row. The bottom right plot gives the vertical resolution computed as z_i/A_{ii}, where z_i is the measurement/retrieval grid

ACPD
14, 18127–18180, 2014

spacing at profile level i, and A_{ii} is the corresponding diagonal element of the averaging kernel matrix; the vertical resolution of the MIPAS retrievals is ~ 4–6 km near the COF_2 profile peak, dropping off outside this range.

4 Global distribution and vertical profiles

For a detailed comparison between ACE-FTS and MIPAS observations, it was decided to focus on one year of measurements between September 2009 and August 2010. Figure 7 provides a comparison between individual profiles for four near-coincident sets of measurements; these are the four closest sets available over this time period. The locations and times of the eight observations can be found in Table 6. The plots also include the a priori profiles, and calculated SLIMCAT profiles for the location and time of each ACE-FTS observation; these calculations will be discussed in Sect. 5. In Fig. 7, the upper altitudes of the ACE-FTS profiles without error bars correspond to the regions where the a priori profiles are scaled in the retrieval (see Sect. 3.2). Although the pairs of measurements were taken at slightly different locations and times of day, near-coincident profiles are expected to be similar but not necessarily identical. COF_2 profiles initially show an increase in VMR with altitude, peaking in the stratosphere and then decreasing with higher altitude; the peak location depends on the latitude and time of year. On the whole, the MIPAS and ACE profiles in Fig. 7 agree well within error bars. The profile for ACE occultation sr34898 (at high northern latitudes in northern winter) shows a dip near 30 km due to part of the profile sampling descended COF_2-poor upper stratospheric air within the polar vortex. The near-coincident MIPAS profile does not show such a strong dip, likely due to the poorer vertical resolution of the MIPAS retrieval.

For the preparation of monthly zonal means over the period September 2009 to August 2010, both ACE and MIPAS datasets were filtered to remove those observations deemed "bad". Due to the relatively poor global coverage of ACE observations over this time period, filtering had to be performed carefully; in this case only significant outliers

ACPD
14, 18127–18180, 2014

were removed. The MIPAS dataset contains substantially more observations over the globe, and as discussed earlier, profile levels with random errors larger than 70 % of the retrieved VMRs were discarded. For each month, a global spike test was applied to all the remaining data. At each altitude the mean and standard deviation of the ensemble were calculated. Any MIPAS profiles with one or more VMRs outside 5σ of the mean VMRs were discarded. This spike test was repeated until all remaining MIPAS profiles were within this 5σ range.

MIPAS observations indicate a minor diurnal variation in COF_2 VMRs, below the measurement error. In this work ACE and MIPAS zonal means were produced without any consideration of the local solar time of the individual measurements. Figure 8 provides a direct side-by-side comparison of MIPAS and ACE zonal means for each of the twelve months, revealing the seasonal variation in the COF_2 distribution. The plotted VMRs are the averages for each month of all filtered data at each altitude within 5° latitude bins. The highest COF_2 VMRs appear at ~ 35 km altitude over the tropics, which receive the highest insolation due to the small solar zenith angle; these peaks are located ~ 10° S for December to April, and ~ 10° N for June to October. COF_2 has a lifetime of ~ 3.8 years (calculated from SLIMCAT; refer to Sect. 5) and is transported polewards by the Brewer–Dobson circulation. As can be seen in the figure, the plots are not symmetric about the equator; an additional peak at southern high latitudes is most prominent in January/February 2010. The observations in Fig. 8 also demonstrate the presence of a strong Southern Hemisphere (SH) polar vortex in September 2009 and August 2010; the associated low COF_2 VMRs at high southern latitudes are a consequence of the descent of air in the vortex from the upper stratosphere/lower mesosphere where COF_2 VMRs are very low. The break-up of the SH polar vortex occurs around November 2009 and begins to form again around June 2010. The Northern Hemisphere (NH) polar vortex is intrinsically weaker and varies considerably from year to year. For the year analysed here the vortex appeared strongest in December 2009 and January 2010. The overall atmospheric distribution of COF_2 is determined by a complicated combination of its production, lifetime, and transport.

ACPD
14, 18127–18180, 2014

More details on these atmospheric processes will be discussed in Sect. 5, along with a discussion of the SLIMCAT CTM.

Since there are only a maximum of 30 ACE-FTS profiles measured per day, compared to ~ 1300 for MIPAS (OR27), the global coverage of the ACE observations between September 2009 and August 2010 is poorer and noisier in appearance, particularly in the tropics. Despite this, the ACE observations agree well with MIPAS, apart from the apparent high bias in the MIPAS VMRs, which will be discussed later in this section. As examples, note the good agreement at mid- to high-latitudes in the SH between regions with high VMRs in December 2009 and March 2010, and low VMRs in August 2010; in the tropical regions, high VMRs peaking north of the equator in October 2009 and August 2010, and south of the equator in February 2010; at mid- to high-latitudes in the NH between regions with high VMRs in September 2009, and low VMRs in February and March 2010.

Since zonal mean plots do not provide an indication of measurement errors, a representative set of individual latitude bins are plotted in Fig. 9 with error bars; all errors are defined as the standard errors of the bin means. Such plots are useful to inspect biases between datasets. Note that SLIMCAT calculations are also included in this figure; these will be further discussed in Sect. 5. ACE random errors are largest close to the tropics at the highest altitudes of the retrieval (where the black error bars are longest). At these altitudes COF_2 features in ACE-FTS spectra are weaker, so the relative noise contribution to the retrieved VMRs is larger. The retrieved ACE VMR profiles at these altitudes have a rather flat appearance, whereas the corresponding MIPAS profiles are peaked. The MIPAS VMRs themselves are biased as much as 30 % higher than ACE, although there is overlap between the error bars. At the very highest altitudes (above ~ 50 km), the ACE VMRs drop to zero, and the MIPAS VMRs approach ~ 50 ppt; these differences result from the different a priori profiles used for the two retrieval schemes. A more detailed discussion on this point will be made in Sect. 5. Figure 9 also reveals a bias at high latitudes in the summer, where the ACE and MIPAS profiles peak just above 30 km. (The summer SH high-latitude peak corresponds to a secondary maxi-

ACPD
14, 18127–18180, 2014

mum in the VMR distribution; the origin of this will be discussed in Sect. 5.) As in the tropics, MIPAS VMRs at the peak are ∼ 30 % higher than ACE. Note that for these particular months, the ACE-FTS was taking many measurements at high latitudes, hence the smaller error bars.

5 Comparison with SLIMCAT 3-D chemical transport model

ACE and MIPAS observations have been compared with output from the SLIMCAT off-line 3-D CTM. SLIMCAT calculates the abundances of a number of stratospheric gases from prescribed source-gas surface boundary conditions and a detailed treatment of stratospheric chemistry, including the major species in the O_x, NO_y, HO_x, Cl_y and Br_y chemical families (e.g. Chipperfield, 1999; Feng et al., 2007). The model uses winds from meteorological analyses to specify horizontal transport while vertical motion in the stratosphere is calculated from diagnosed heating rates. This approach gives a realistic stratospheric circulation (Chipperfield, 2006; Monge-Sanz et al., 2007). The troposphere is assumed to be well-mixed.

For this study SLIMCAT was integrated from 2000 to 2012 at a horizontal resolution of 5.6° × 5.6° and 32 levels from the surface to 60 km. The model uses a $\sigma - \theta$ vertical coordinate (Chipperfield, 2006) and was forced by European Centre for Medium Range Weather Forecasts (ECMWF) reanalyses (ERA-Interim from 1989 onwards). The volume mixing ratios of source gases at the surface level were specified using data files compiled for the 2010 WMO ozone assessment (WMO/UNEP, 2011). These global mean surface values define the long-term tropospheric source gas trends in the model.

A previous run of SLIMCAT, used in an investigation of the atmospheric trends of halogen-containing species measured by the ACE-FTS (Brown et al., 2011), neglected the COF_2 contribution from the atmospheric degradation of HFCs. This has now been remedied for the most important HFCs. In total, this run of SLIMCAT calculates COF_2 contributions arising from the degradation of CFC-12, CFC-113, CFC-114, CFC-115,

ACPD
14, 18127–18180, 2014

HCFC-22, HCFC-142b, HFC-23, HFC-134a, HFC-152a, Halon 1211, and Halon 1301. A number of these molecules, e.g. HFC-23, are included even though they make no appreciable contribution to the formation of COF_2 compared with the major source gases. Some other HFCs, e.g. HFC-125, which similarly make minimal contribution, are not included in the model. In addition to providing a direct comparison with satellite observations, the new SLIMCAT calculations have been used to show where COF_2 is produced and which source gases have produced it. Most COF_2 is produced in the tropics where solar insolation is highest. Figure 10 provides plots of the loss rates (annual mean zonal mean; pptv day^{-1}) for the three main source gases which produce COF_2. As can be seen, the largest contributing COF_2 source at ~ 30–35 km is CFC-12, followed by CFC-113 (approximately a factor of 10 smaller). HCFC-22 is the second largest contributing source gas overall, however its contribution peaks low in the troposphere (not relevant for stratospheric COF_2) and higher up in the stratosphere (~ 40–45 km). CFC-12 and CFC-113 are removed mainly by photolysis ~ 20–40 km; above this altitude range the abundances of CFC-12 and CFC-113 tend to zero so that they make only a small contribution to the formation of COF_2. On the other hand, HCFC-22 is mainly removed from the atmosphere by reaction with OH. Since this reaction is slower, HCFC-22 persists higher into the stratosphere than CFC-12 and CFC-113 and can therefore lead to COF_2 production in the upper stratosphere and lower mesosphere. Individual contributions from molecules other than these three are typically a small fraction of 1 %. In the altitude region below the maximum COF_2 VMRs at all locations there is net production of COF_2, while at higher altitudes there is net loss. The primary loss of COF_2 in the atmosphere occurs via photolysis, with an additional secondary loss mechanism through reaction with $O(^1D)$. Figure 10 also contains a plot of the COF_2 annual mean zonal total loss rate.

SLIMCAT has also been used to estimate the atmospheric lifetime of COF_2 by simply dividing the total modelled atmospheric burden by the total calculated atmospheric loss rate. The total calculated mean atmospheric lifetime is ~ 3.8 years. This lifetime varies slightly between the hemispheres, 3.76 years in the south and 3.82 years in the north.

ACPD
14, 18127–18180, 2014

In the lower stratosphere COF_2 can be regarded as a long-lived tracer (local lifetime of many years). Therefore, its tracer isopleths follow the typical tropopause-following contours of any long-lived tracer. In this sense, COF_2 is analogous to NO_y which is produced from N_2O. It has been checked as part of this work that a correlation plot of COF_2 with its major source, CFC-12, is compact in the lower stratosphere, at altitudes below the region of COF_2 maxima (Plumb and Ko, 1992).

As discussed in Sect. 4, Fig. 7 contains a comparison between individual ACE-FTS and MIPAS profiles for the measurements specified in Table 6. This figure also contains SLIMCAT profiles calculated for the location and time of each ACE-FTS observation. In comparison with the retrieved portion of the ACE profiles (marked by black error bars), the calculated SLIMCAT VMRs are generally slightly lower; the agreement with MIPAS is worse, however it must be acknowledged that the two sets of measurements are not strictly coincident. Additionally, SLIMCAT captures the VMR "dip" observed for ACE occultation sr34898 (at 67.27° N on the vortex edge, 4 February 2010) near 30 km altitude, confirming that this profile samples air from the polar vortex. This explanation is supported by the corresponding ACE HF profile, which shows an enhancement near 30 km due to the sampling of descended HF-rich upper-stratospheric air from the polar vortex.

Figure 11 provides a comparison between SLIMCAT and ACE zonal means. In order to reduce the noise and increase the latitude coverage for the comparison, the plotted ACE data are monthly averages of the data in Fig. 8 (September 2009 to August 2010) with data from the previous year; on the scale of the Figure there is no significant variation in the seasonal pattern as measured by the ACE-FTS. Figure 11 reveals that the model agrees well with the ACE observations and reproduces very well the significant seasonal variation, although SLIMCAT produces slightly lower VMRs and the ACE measurements still suffer from measurement noise. Comparing the SLIMCAT zonal means (in Fig. 11) with those for MIPAS (in Fig. 8) again demonstrates the good agreement in seasonal variation, but the MIPAS VMRs have a noticeably high bias compared with the model.

ACPD
14, 18127–18180, 2014

Figure 9 shows a representative set of SLIMCAT profiles in 5° latitude bins from the September 2009 to August 2010 time period, along with averaged ACE and MIPAS profiles. These demonstrate a very good agreement between the SLIMCAT calculations and ACE observations, although above ~ 35 km this agreement is somewhat worse, particularly the upper parts of the ACE profiles (without error bars) which are derived from the scaled a priori profile and susceptible to systematic errors (see Sect. 3.2). Whereas the ACE VMRs drop to zero at ~ 55 km, the SLIMCAT VMRs do not reach zero even near the model top level around 60 km due to the calculated ongoing production of COF_2 from HCFC-22 (see Fig. 10). MIPAS VMRs similarly do not drop to zero, principally because the a priori profiles make a larger contribution to the retrieved VMRs at these altitudes. Unfortunately, neither ACE nor MIPAS measurements are able to validate the SLIMCAT model HCFC-22/COF_2 VMRs near 55–60 km.

In autumn when solar heating of the relevant polar region comes to an end, a stratospheric polar vortex begins to form. This is a large-scale region of air contained within a strong westerly jet stream that encircles the polar region. Reaching maximum strength in the middle of winter, the polar vortex decays as sunlight returns to the polar region in the spring. Polar vortices, which extend from the tropopause up into the mesosphere, are quasi-containment vessels for air at cold temperatures and low-ozone content. They play a critical role in polar ozone depletion, more so in the Antarctic, where the vortex is larger, stronger, and longer-lived than in the Arctic. The SLIMCAT September 2009 (09/2009) plot in Fig. 11 demonstrates the presence of a strong SH polar vortex by the low COF_2 VMRs at high southern latitudes; as mentioned earlier this is a consequence of the descent of upper-stratospheric air where COF_2 VMRs are very low. The breakup of the SH polar vortex as simulated by SLIMCAT occurs around November 2009 (11/2009) and begins to form again around June 2010 (06/2010). On the other hand, the descent of upper stratospheric air corresponding to the onset of the NH polar vortex is less obvious due to the intrinsically lower COF_2 VMRs in the NH summer; SLIMCAT observations suggest the northern polar vortex is present from December 2009 to January 2010.

ACPD
14, 18127–18180, 2014

Although some of the COF_2 present at mid- and high-latitudes can be attributed to transport of COF_2-rich tropical air via the Brewer–Dobson circulation (a slow upwelling of stratospheric air in the tropics, followed by poleward drift through the mid-latitudes, and descent in the mid- and high-latitudes), this cannot account for the secondary maximum in VMR (~ 31 km) present in the SH polar region for which an atmospheric chemistry explanation is needed. Diagnosis of the model rates shows that in summer, photochemical production of COF_2 extends to the pole in the middle stratosphere (i.e. in polar day). Further diagnosis of the first-order loss rates of the main COF_2 precursors shows that photolysis and reactions with $O(^1D)$ are symmetrical between the hemispheres. The only precursor loss reaction which shows significant hemispheric asymmetry is the temperature-dependent reaction of CHF_2Cl (HCFC-22) + OH. As the SH polar summer mid-stratosphere is around 10 K warmer than the corresponding location in the NH, this reaction provides a stronger source of COF_2 in SH summer compared to the Arctic and contributes to this secondary maximum. Indeed, in a model sensitivity run where the production of COF_2 from HCFC-22 was switched off, this secondary SH summer peak disappeared. While the first-order loss rates of the COF_2 source gas precursors are generally symmetrical between the hemispheres, this is not true for the source gases themselves. Differences in the meridional Brewer–Dobson circulation, with stronger mixing to the pole in the north and stronger descent in the south, lead to differences in the distribution of COF_2 precursors. This leads to differences in COF_2 production resulting in the observed and modelled hemispheric asymmetry in COF_2 at middle latitudes.

6 Trends

As mentioned in the introduction, there is evidence that the atmospheric abundance of COF_2 is increasing with time (Duchatelet et al., 2009; Brown et al., 2011). Although the atmospheric abundances of COF_2 source gases such as CFC-12 and CFC-113 are currently decreasing, HCFC-22 and the minor HFC contributors are still on the

ACPD
14, 18127–18180, 2014

increase. Figure 1–1 of the 2010 WMO ozone assessment (WMO/UNEP, 2011) shows the trends in mean global surface mixing ratios for these two species during the 1990–2009 time period. The CFC-12 growth rate is observed to reduce slowly from 1990, plateauing around 2003–2004, after which it becomes negative, i.e. an overall loss of CFC-12. In comparison, the growth rate of HCFC-22 has been relatively constant since 1990, with a slight increase in growth rate occurring around 2007.

A number of previous studies have quantified the trend in atmospheric COF_2 over time. For the Jungfraujoch 1985 to 1995 time series (46.5° N latitude, 8.0° E longitude), a period when CFC-12 was still increasing the atmosphere, an average COF_2 linear trend of $4.0 \pm 0.5\,\%\,year^{-1}$ was derived (Mélen et al., 1998). COF_2 trends from more recent studies are considerably lower, largely due to the phase out of its principal source gas, CFC-12. A trend of $0.8 \pm 0.4\,\%\,year^{-1}$ has recently been derived from ACE data for 2004 to 2010 (Brown et al., 2011). Since the majority of halogenated source gases reach the stratosphere by upwelling through the tropical tropopause region, the ACE COF_2 trend was determined by averaging measurements in the latitude band 30° S to 30° N between 30 and 40 km altitude; effectively the seasonal variation in COF_2 was averaged out. For the Jungfraujoch 2000 to 2007 time series, a linear trend of $0.4 \pm 0.2\,\%\,year^{-1}$ was derived (Duchatelet et al., 2009). The observed COF_2 seasonal variation, which was removed using a cosine function, had maxima towards the end of February (winter) and minima in late summer when photodissociation processes are at their maximum. In contrast, trends calculated from older SLIMCAT runs for Brown et al. (2011) and Duchatelet et al. (2009) are $-1.3 \pm 0.4\,\%\,year^{-1}$ and $-0.5 \pm 0.2\,\%\,year^{-1}$, respectively. For the latter of these, it was noted that the SLIMCAT time series suffered from several discontinuities in the operational ECMWF meteorological data, for which the vertical resolution had been changed several times; this resulted in a decrease in the SLIMCAT COF_2 columns between 2002 and 2006. For the present work, this is no longer a problem because ERA-Interim reanalyses, which use a consistent version of the ECMWF model, are now used by SLIMCAT.

ACPD
14, 18127–18180, 2014

In this section, ACE and MIPAS time series are derived as a function of altitude and latitude. As discussed previously, e.g. in Harrison and Bernath (2013), ACE latitude coverage is uneven. For data between January 2004 and September 2010 (the last month for which ACE v3.0 data is usable), the 18 10° latitude bins used for the ACE time series contain, from southernmost to northernmost, 1000, 1323, 5265, 1776, 796, 608, 482, 420, 390, 394, 339, 413, 650, 1062, 2012, 4828, 1875, 1315 occultations, respectively, i.e. over three-quarters of the measurements lie in latitude bins poleward of 50° S/N. On the other hand, MIPAS data coverage over the globe is more even and extensive, apart from some periods during 2004–2006 when nominal mode measurements were not made.

Figure 12 illustrates the MIPAS and SLIMCAT time series for COF_2 between July 2002 and April 2012 for all latitudes at selected altitudes; both datasets were binned in 10° latitude bands. (Due to the sparse nature of the ACE-FTS measurements, such a plot has not been provided for the ACE dataset.) An annual cycle is readily observed, and as expected its phase is opposite in each hemisphere. The amplitude of this cycle is largest near the poles; note that the maxima in the plot at 20.5 km altitude correspond to the descent of COF_2 in winter polar vortices. Close inspection of Fig. 12, particularly the plots above 30 km, also reveals the presence of the quasi-biennial oscillation (QBO) signal, which is strongest in the tropics. Overall, there is good agreement between the MIPAS and SLIMCAT plots in terms of the overall latitude–altitude pattern, however, as noted before, the MIPAS VMRs are biased high; for example, maxima over the tropics as much as ∼ 25 % and maxima near the poles as much as ∼ 50 %.

Figure 13 provides the time series for five altitude–latitude bin combinations of ACE, MIPAS and SLIMCAT data; for ease of viewing, this plot does not include errors. In all plots, the main features in the time series agree well. Note the observed QBO signal for all three datasets, stronger in the two tropical plots and weaker in the high-northern-latitude plot. In the top two plots of Fig. 13 MIPAS is biased high, although less so at 20.5 km. As established previously (refer to Fig. 9), this is a feature of the MIPAS dataset at the high southern latitudes. The agreement between ACE and SLIMCAT is

ACPD
14, 18127–18180, 2014

somewhat better, agreeing within the errors of the ACE data, although less so at high southern latitudes.

COF_2 trends at each altitude for all 18 latitude bins have been calculated from monthly percentage anomalies in COF_2 zonal means, $C^{z,\theta}(n)$, defined as

$$C^{z,\theta}(n) = 100\frac{\mathrm{VMR}^{z,\theta}(n) - \sum_{m=1}^{12} \delta_{nm}\overline{\mathrm{VMR}}^{z,\theta}(m)}{\sum_{m=1}^{12} \delta_{nm}\overline{\mathrm{VMR}}^{z,\theta}(m)}, \quad (7)$$

where n is a running index from month zero to 80 (January 2004 to September 2010), $\mathrm{VMR}^{z,\theta}(n)$ is the corresponding mixing ratio at altitude z and latitude θ, $\overline{\mathrm{VMR}}^{z,\theta}(m)$ is the average of all zonal means for each of the twelve months, m, and δ_{nm}, although not used in its strict mathematical sense, is one when index n corresponds to one of the months m and is zero otherwise. In order to compare the three datasets, the same time period was used for each analysis. Such an approach essentially removes the annual cycle and the effect of biases in VMRs; the trend is simply equated to the "slope" of the linear regression between $C^{z,\theta}(n)$ and the dependent variable $n/12$. The inclusion of additional terms such as the annual cycle and its harmonics resulted in no additional improvement in the regression.

Figure 14 presents the annual percentage trends (January 2004 to September 2010) for ACE, MIPAS, and SLIMCAT as a function of latitude and altitude. The plotting range has been chosen to cover the maximum VMR features in the COF_2 global distributions; this broadly follows the upper altitude range of the actual ACE retrievals and removes portions of the MIPAS profiles which have the largest contributions from the a priori profile. Note that whereas the MIPAS time series used to derive trends contains data for 67 distinct months in all latitudes band, the number of months of ACE data available varies from as low as 15 to as high as 63 in each latitude band. Errors were not explicitly treated in the linear regression of the SLIMCAT outputs, but were for the MIPAS and

ACPD
14, 18127–18180, 2014

ACE VMRs. Note that as the MIPAS and ACE trends approach zero, the ratio to their 1σ uncertainties drops well below one. Broadly speaking, the trends for any ACE/MIPAS latitude–altitude region in Fig. 14 which appear predominantly blue or green become more statistically significant when the individual contributions are averaged.

The MIPAS plot in Fig. 14 indicates that between 2004 and 2010, COF_2 has increased most rapidly (approaching ~ 4 % per year) at altitudes above ~ 25 km in the southern latitudes and at altitudes below ~ 25 km in the northern latitudes. The ACE plot broadly agrees with respect to these two regions of largest positive trend, although their magnitudes are slightly lower. Additionally, the ACE trends in the tropical region are predominantly negative, which somewhat agrees with SLIMCAT below 25 km.

The SLIMCAT plot contains a number of features which agree with both the MIPAS and ACE plots. In particular, the SLIMCAT plot indicates a decrease in COF_2 in the tropical region (between 20° S and 10° N), although the largest decrease occurs at ~ 27 km and 0° latitude; ACE agrees better than MIPAS in this region, except for a narrow altitude range ~ 30 km where the ACE trends are slightly positive. Outside the tropics, the SLIMCAT plot agrees better with MIPAS, in particular for the regions of largest positive trends which occur at high southern latitudes above 30 km and northern latitudes below ~ 25 km.

An additional SLIMCAT run has been performed with dynamics arbitrarily fixed to those for the year 2000; results from this run give a "clean" COF_2 signal without the complication of changes in stratospheric dynamics. Trends have been calculated in the same manner as above, and plotted in the lowest panel of Fig. 14. Compared with trends for the "control" SLIMCAT run, those for the fixed-dynamics run lie predominantly between 0 and 1 %, with a relatively uniform distribution throughout the stratosphere. This indicates that the variations in SLIMCAT trends, and by extension the regions of agreement with MIPAS and ACE, result from changes in stratospheric dynamics between January 2004 and September 2010.

One might expect that the decreasing SLIMCAT trends over the 2004–2010 period in the lower tropical stratosphere, where the air is youngest, result directly from

ACPD
14, 18127–18180, 2014

the decrease in mean global surface mixing ratio of CFC-12 since ∼2003–2004 (WMO/UNEP, 2011); note that HCFC-22 produces COF_2 at higher altitudes. However, the absence of any negative tropical trends in the fixed-dynamics SLIMCAT plot indicates that this feature must result from dynamical considerations.

The analyses used to force the SLIMCAT calculations provide information on the stratospheric circulation, but do not allow for any rigorous explanation of the changing stratospheric dynamics that are responsible for the observed trends. Interestingly, the two regions of large positive trends in the ACE, MIPAS, and SLIMCAT plots correspond quite well to the regions of positive age of air trends, as reported by Stiller et al. (2012); see Fig. 10. Additionally, the region of positive trends in the tropics ∼28–35 km, contained in the ACE plot, more-or-less agrees with the corresponding feature in the age-of-air-trend plot. As discussed by Stiller et al. (2012), it is likely that variations in atmospheric mixing have occurred over the observation period. The regions of maximum COF_2 trends must result from increased in-mixing of COF_2-rich air, possibly due to major sudden stratospheric mid-winter warmings. The negative trends in the tropics could result from an increase in the rate of upwelling over the observation period.

Overall global trends in COF_2 VMRs, weighted by the average VMRs at each altitude and latitude, have been calculated from the three datasets using errors in trends as determined from the linear regression; $0.30 \pm 0.44\,\%\,\text{year}^{-1}$ for ACE, $0.85 \pm 0.34\,\%\,\text{year}^{-1}$ for MIPAS, and $0.88\,\%\,\text{year}^{-1}$ for SLIMCAT. Note that these values only apply to the January 2004 to September 2010 time period. Any spectroscopic deficiencies that might lead to regional biases in the ACE and MIPAS datasets should have been removed by taking percentage anomalies, however there still remains the possibility of systematic errors that contribute to time-dependent biases. The pressure-temperature retrievals for ACE v3.0 processing assume a rate of increase of $1.5\,\text{ppm}\,\text{year}^{-1}$ for the CO_2 VMRs, which are assumed to have a single profile shape for all locations and seasons. This rate of increase is lower than the accepted value of $1.90–1.95\,\text{ppm}\,\text{year}^{-1}$ ($0.5\,\%\,\text{year}^{-1}$) as used, for example, in IG2 CO_2 profiles for MIPAS retrievals. By the end of the time series, ACE v3.0 CO_2 VMRs are too low by ∼0.7 %. This translates

ACPD
14, 18127–18180, 2014

into a small time-dependent negative bias in COF_2 VMR, meaning that the trend derived from ACE v3.0 data is biased low by on average $\sim 0.1\,\%\,year^{-1}$, although it is not obvious how the bias varies with latitude and altitude.

Plans are currently underway to create a new ACE processing version 4.0, in which it is assumed that the CO_2 VMR increases by $0.5\,\%\,year^{-1}$ and in which age of air considerations are used to generate the vertical CO_2 VMR profile as a function of latitude and time of year (Toon, personal communication, 2012). It is anticipated that the new v4.0 will enable more accurate trends to be derived. The ACE-FTS continues to take atmospheric measurements from orbit, with only minor loss in performance; it will be possible to extend the COF_2 time series to the present day and beyond.

7 Conclusions

Carbonyl fluoride (COF_2) is the second most abundant "inorganic" fluorine reservoir in the stratosphere with main sources being the atmospheric degradation of CFC-12 (CCl_2F_2), HCFC-22 (CHF_2Cl), and CFC-113 ($CF_2ClCFCl_2$), species whose emissions are predominantly anthropogenic.

This work reports the first global distributions of carbonyl fluoride in the Earth's atmosphere using infrared satellite remote-sensing measurements by the ACE-FTS, which has been recording atmospheric spectra since 2004, and the MIPAS instrument, which has recorded thermal emission atmospheric spectra between 2002 and 2012. The observations reveal a high degree of seasonal and latitudinal variability over the course of a year, and agree well with the output of the SLIMCAT model, although MIPAS VMRs are biased high by as much as $\sim 30\,\%$.

The maximum in the COF_2 VMR distribution occurs at ~ 30–$35\,km$ altitude in the tropics where solar insolation is highest; this region is dominated by COF_2 formed from the photolysis of CFC-12 and CFC-113. The first-order loss rates of the main COF_2 precursors are symmetrical between the hemispheres, except for the HCFC-22 + OH reaction, which is temperature dependent; a secondary maximum at ~ 25–$30\,km$

ACPD
14, 18127–18180, 2014

altitude is present at high latitudes in SH summer due to the mid-stratosphere being around 10 K warmer than the corresponding location in the NH summer. There is also asymmetry in the distribution of COF_2 precursors due to differences in the meridional Brewer–Dobson circulation, with stronger mixing to the pole in the north and stronger descent in the south; this results in larger VMRs at mid- and high-latitudes in the SH.

Between January 2004 and September 2010 COF_2 grew most rapidly at altitudes above ∼ 25 km in the southern latitudes and at altitudes below ∼ 25 km in the northern latitudes, whereas it declined most rapidly in the tropics. These variations are attributed to changes in stratospheric dynamics over the observation period. The overall COF_2 global trend over this period is calculated as $0.85 \pm 0.34\,\%\,year^{-1}$ (MIPAS), $0.30 \pm 0.44\,\%\,year^{-1}$ (ACE), and $0.88\,\%\,year^{-1}$ (SLIMCAT).

Author contribution

Based on an idea from P. F. B., J. J. H. devised the study and performed the data analysis. A. D. performed the MIPAS retrievals and S. C. filtered and prepared the data for analysis. C. D. B. performed the ACE-FTS retrievals and J. J. H. filtered and prepared the data for analysis. P. F. B. allowed the use of ACE data in this work. M. P. C. and S. D. ran the SLIMCAT model and provided additional explanation of the outputs. J. J. H. prepared the manuscript with contributions from M. P. C. and A. D.

Acknowledgements. The authors wish to thank the Natural Environment Research Council (NERC) for supporting J. J. H. through grant NE/I022663/1. The ACE satellite mission is funded primarily by the Canadian Space Agency (CSA).

References

Bernath, P. F., McElroy, C. T., Abrams, M. C., Boone, C. D., Butler, M., Camy-Peyret, C., Carleer, M., Clerbaux, C., Coheur, P.-F., Colin, R., DeCola, P., DeMazière, M., Drummond, J. R., Dufour, D., Evans, W. F. J., Fast, H., Fussen, D., Gilbert, K., Jennings, D. E., Llewellyn, E. J.,

ACPD
14, 18127–18180, 2014

Lowe, R. P., Mahieu, E., McConnell, J. C., McHugh, M., McLeod, S. D., Michaud, R., Midwinter, C., Nassar, R., Nichitiu, F., Nowlan, C., Rinsland, C. P., Rochon, Y. J., Rowlands, N., Semeniuk, K., Simon, P., Skelton, R., Sloan, J. J., Soucy, M.-A., Strong, K., Tremblay, P., Turnbull, D., Walker, K. A., Walkty, I., Wardle, D. A., Wehrle, V., Zander, R., and Zou, J.: Atmospheric Chemistry Experiment (ACE): mission overview, Geophys. Res. Lett., 32, L15S01, doi:10.1029/2005GL022386, 2005.

Boone, C. D., Walker, K. A., and Bernath, P. F.: Version 3 retrievals for the Atmospheric Chemistry Experiment Fourier Transform Spectrometer (ACE-FTS), in: The Atmospheric Chemistry Experiment ACE at 10: a Solar Occultation Anthology, edited by: Bernath, P. F., A. Deepak Publishing, Hampton, Virginia, USA, 103–127, available at http://acebox2.uwaterloo.ca/publications/2013/Version3.5retreivals2013.pdf (last access: 1 July 2014), 2013.

Brown, A. T., Chipperfield, M. P., Boone, C., Wilson, C., Walker, K. A., and Bernath, P. F.: Trends in atmospheric halogen containing gases since 2004, J. Quant. Spectrosc. Ra., 112, 2552–2566, 2011.

Brown, A. T., Chipperfield, M. P., Richards, N. A. D., Boone, C., and Bernath, P. F.: Global stratospheric fluorine inventory for 2004–2009 from Atmospheric Chemistry Experiment Fourier Transform Spectrometer (ACE-FTS) measurements and SLIMCAT model simulations, Atmos. Chem. Phys., 14, 267–282, doi:10.5194/acp-14-267-2014, 2014.

Chipperfield, M. P.: Multiannual simulations with a three-dimensional chemical transport model, J. Geophys. Res., 104, 1781–1805, doi:10.1029/98jd02597, 1999.

Chipperfield, M. P.: New version of the TOMCAT/SLIMCAT off-line chemical transport model: intercomparison of stratospheric tracer experiments, Q. J. Roy. Meteor. Soc., 132, 1179–1203, 2006.

Duchatelet, P., Mahieu, E., Ruhnke, R., Feng, W., Chipperfield, M., Demoulin, P., Bernath, P., Boone, C. D., Walker, K. A., Servais, C., and Flock, O.: An approach to retrieve information on the carbonyl fluoride (COF_2) vertical distributions above Jungfraujoch by FTIR multispectrum multi-window fitting, Atmos. Chem. Phys., 9, 9027–9042, doi:10.5194/acp-9-9027-2009, 2009.

Duchatelet, P., Demoulin, P., Hase, F., Ruhnke, R., Feng, W., Chipperfield, M. P., Bernath, P. F., Boone, C. D., Walker, K. A., and Mahieu, E.: Hydrogen fluoride total and partial column time series above the Jungfraujoch from long-term FTIR measurements: impact of the line-shape model, characterization of the error budget and seasonal cycle, and comparison with satellite and model data, J. Geophys. Res., 115, D22306, doi:10.1029/2010JD014677, 2010.

ACPD
14, 18127–18180, 2014

Feng, W., Chipperfield, M. P., Dorf, M., Pfeilsticker, K., and Ricaud, P.: Mid-latitude ozone changes: studies with a 3-D CTM forced by ERA-40 analyses, Atmos. Chem. Phys., 7, 2357–2369, doi:10.5194/acp-7-2357-2007, 2007.

Fischer, H., Birk, M., Blom, C., Carli, B., Carlotti, M., von Clarmann, T., Delbouille, L., Dudhia, A., Ehhalt, D., Endemann, M., Flaud, J. M., Gessner, R., Kleinert, A., Koopman, R., Langen, J., López-Puertas, M., Mosner, P., Nett, H., Oelhaf, H., Perron, G., Remedios, J., Ridolfi, M., Stiller, G., and Zander, R.: MIPAS: an instrument for atmospheric and climate research, Atmos. Chem. Phys., 8, 2151–2188, doi:10.5194/acp-8-2151-2008, 2008.

Flaud, J.-M., Brizzi, G., Carlotti, M., Perrin, A., and Ridolfi, M.: MIPAS database: Validation of HNO_3 line parameters using MIPAS satellite measurements, Atmos. Chem. Phys., 6, 5037–5048, doi:10.5194/acp-6-5037-2006, 2006.

Gribble, G. W.: Naturally occurring organofluorines, in: Handbook of Environmental Chemisty, vol. 3, Part N: Organofluorines, edited by: Neilson, A. H., Springer-Verlag, Berlin, Heidelberg, 2002.

Harrison, J. J. and Bernath, P. F.: ACE-FTS observations of acetonitrile in the lower stratosphere, Atmos. Chem. Phys., 13, 7405–7413, doi:10.5194/acp-13-7405-2013, 2013.

Hartmann, J. M., Boulet, C., and Robert, D.: Collisional Effects on Molecular Spectra, Laboratory Experiments and Models, Consequences for Applications, Elsevier, Oxford, 2008.

Irion, F. W., Gunson, M. R., Toon, G. C., Chang, A. Y., Eldering, A., Mahieu, E., Manney, G. L., Michelsen, H. A., Moyer, E. J., Newchurch, M. J., Osterman, G. B., Rinsland, C. P., Salawitch, R. J., Sen, B., Yung, Y. L., and Zander, R.: Atmospheric Trace Molecule Spectroscopy (ATMOS) Experiment Version 3 data retrievals, Appl. Optics, 41, 6968–6979, 2002.

May, R. D.: Line intensities and collisional-broadening parameters for the v_4 and v_6 bands of carbonyl fluoride, J. Quant. Spectrosc. Ra., 48, 701–712, 1992.

Mélen, F., Mahieu, E., Zander, R., Rinsland, C. P., Demoulin, P., Roland, G., Delbouille, L., and Servais, C.: Vertical column abundances of COF_2 above the Jungfraujoch Station, derived from ground-based infrared solar observations, J. Atmos. Chem., 29, 119–134, 1998.

Monge-Sanz, B. M., Chipperfield, M. P., Simmons, A. J., and Uppala, S. M.: Mean age of air and transport in a CTM: comparison of different ECMWF analyses, Geophys. Res. Lett., 34, L04801, doi:10.1029/2006gl028515, 2007.

Plumb, R. A. and Ko, M. K. W.: Interrelationships between mixing ratios of long-lived stratospheric constituents, J. Geophys. Res., 97, 10145–10156, 1992.

ACPD
14, 18127–18180, 2014

Remedios, J. J., Leigh, R. J., Waterfall, A. M., Moore, D. P., Sembhi, H., Parkes, I., Greenhough, J., Chipperfield, M.P., and Hauglustaine, D.: MIPAS reference atmospheres and comparisons to V4.61/V4.62 MIPAS level 2 geophysical data sets, Atmos. Chem. Phys. Discuss., 7, 9973–10017, doi:10.5194/acpd-7-9973-2007, 2007.

Ricaud, P. and Lefevre, F.: Fluorine in the atmosphere, in: Fluorine and the Environment: Atmospheric Chemistry, Emissions, & Lithosphere, edited by: Tressaud, A., Elsevier, Oxford, UK, 2006.

Rinsland, C. P., Zander, R., Brown, L. R., Farmer, C. B., Park, J. H., Norton, R. H., Russell, III, J. M., and Raper, O. F.: Detection of carbonyl fluoride in the stratosphere, Geophys. Res. Lett., 13, 769–772, 1986.

Rodgers, C. D.: Inverse methods for atmospheric sounding: theory and Practice, Volume 2 of Series on Atmospheric, Oceanic and Planetary Physics, World Scientific Co. Pte. Ltd., Singappore, 2000.

Rothman, L., Jacquemart, D., Barbe, A., Benner, C. D., Birk, M., Brown, L. R., Carleer, M. R., Chackerian Jr., C., Chance, K., Coudert, L. H., Dana, V., Devi, V. M., Flaud, J.-M., Gamache, R. R., Goldman, A., Hartmann, J.-M., Jucks, J. W., Maki, A. G., Mandin, J.-Y., Massie, S. T., Orphal, J., Perrin, A., Rinsland, C. P., Smith, M., Tennyson, J., Tolchenov, R. N., Toth, R. A., Vander Auwera, J., Varanasi, P., and Wagner, G.: The HITRAN 2004 molecular spectroscopic database, J. Quant. Spectrosc. Ra., 96, 193–204, 2005.

Sharpe, S. W., Johnson, T. J., Sams, R. L., Chu, P. M., Rhoderick, G. C., and Johnson, P. A.: Gas-phase databases for quantitative infrared spectroscopy, Appl Spectrosc., 58, 1452–1461, 2004.

Spang, R., Remedios, J. J., and Barkley, M.: Colour indices for the detection and differentiation of cloud types in infra-red limb emission spectra, Adv. Space Res., 33, 1041–1047, 2004.

Stiller, G. P., von Clarmann, T., Haenel, F., Funke, B., Glatthor, N., Grabowski, U., Kellmann, S., Kiefer, M., Linden, A., Lossow, S., and López-Puertas, M.: Observed temporal evolution of global mean age of stratospheric air for the 2002 to 2010 period, Atmos. Chem. Phys., 12, 3311–3331, doi:10.5194/acp-12-3311-2012, 2012.

Velazco, V. A., Toon, G. C., Blavier, J.-F. L., Kleinböhl, A., Manney, G. L., Daffer, W. H., Bernath, P. F., Walker, K. A., and Boone, C.: Validation of the atmospheric chemistry experiment by noncoincident MkIV balloon profiles, J. Geophys. Res., 116, D06306, doi:10.1029/2010jd014928, 2011.

ACPD
14, 18127–18180, 2014

WMO/UNEP: Scientific Assessment of Ozone Depletion: 2010, Global Ozone Research and Monitoring Project-Report No. 52, 516 pp., Geneva, Switzerland, 2011.

Zander, R., Rinsland, C. P., Mahieu, E., Gunson, M. R., Farmer, C. B., Abrams, M. C., and Ko, M. K. W.: Increase of carbonyl fluoride (COF_2) in the stratosphere and its contribution to the 1992 budget of inorganic fluorine in the upper stratosphere, J. Geophys. Res., 99, 16737–16743, 1994.

ACPD

14, 18127–18180, 2014

Table 1. Microwindows for the v3.0 ACE-FTS carbonyl fluoride retrieval.

Centre frequency (cm^{-1})	Microwindow width (cm^{-1})	Lower altitude (km)	Upper altitude (km)
1234.70	1.40	12	$45 - 11\sin^2$ (latitude°)
1236.90	1.40	25	$45 - 11\sin^2$ (latitude°)
1238.00	0.80	15	$45 - 11\sin^2$ (latitude°)
1239.90	1.00	15	$45 - 11\sin^2$ (latitude°)
1930.60	1.40	$15 - 3\sin^2$ (latitude°)	$45 - 11\sin^2$ (latitude°)
1936.48	0.65	12	$45 - 11\sin^2$ (latitude°)
1938.15	1.50	30	$35 - 6\sin^2$ (latitude°)
1939.55	1.20	30	$35 - 6\sin^2$ (latitude°)
1949.40	1.20	15	$45 - 11\sin^2$ (latitude°)
1950.70	0.50	12	$45 - 11\sin^2$ (latitude°)
1952.23	1.00	12	$45 - 11\sin^2$ (latitude°)
2672.70[a]	0.60	12	20

[a] Included to improve results for interferer HDO.

ACPD
14, 18127–18180, 2014

Table 2. Interferers in the v3.0 ACE-FTS carbonyl fluoride retrieval.

Molecule	Lower altitude limit (km)	Upper altitude limit (km)
H_2O	12	$45 - 11\sin^2$ (latitude°)
CO_2	12	$45 - 11\sin^2$ (latitude°)
CH_4	12	$45 - 11\sin^2$ (latitude°)
NO	12	$45 - 11\sin^2$ (latitude°)
$^{13}CH_4$	12	$45 - 11\sin^2$ (latitude°)
$OC^{18}O$	12	$45 - 11\sin^2$ (latitude°)
N_2O	12	$45 - 11\sin^2$ (latitude°)
$N_2^{18}O$	12	$32 - 2\sin^2$ (latitude°)
^{15}NNO	12	$27 - 2\sin^2$ (latitude°)
HDO	12	24
CH_3D	12	23

ACPD
14, 18127–18180, 2014

Table 3. Microwindows for the MIPAS carbonyl fluoride retrieval.

Centre frequency (cm^{-1})	Microwindow width (cm^{-1})	Lower altitude (km)	Upper altitude (km)
773.5000	3.0000	18.0	43.0
1223.9375	3.0000	10.5	54.0
1227.21875	2.9375	16.5	46.0
1231.8750	3.0000	12.0	40.0
1234.7500	2.1250	7.5	19.5

ACPD
14, 18127–18180, 2014

Table 4. Interferers in the MIPAS carbonyl fluoride retrieval.

Molecule	Lower altitude limit (km)	Upper altitude limit (km)
H_2O	7.5	54.0
CO_2	7.5	54.0
O_3	7.5	54.0
N_2O	7.5	54.0
CH_4	7.5	54.0
NO_2	18.0	43.0
HNO_3	10.5	54.0
NH_3	18.0	43.0
HOCl	7.5	54.0
HCN	18.0	43.0
H_2O_2	7.5	54.0
CCl_4	18.0	43.0
$ClONO_2$	18.0	43.0
N_2O_5	7.5	46.0

ACPD
14, 18127–18180, 2014

Table 5. Sources of systematic uncertainty in the ACE-FTS v3.0 carbonyl fluoride retrieval.

Source	Symbol	Fractional value
COF_2 spectroscopy	μ_{spec}	0.15
Spectral interferers	μ_{int}	0.01
Temperature	μ_T	0.04
Altitude	μ_z	0.04
ILS	μ_{ILS}	0.01

ACPD
14, 18127–18180, 2014

Table 6. Near-coincident ACE-FTS and MIPAS measurements.

Date	ACE-FTS Occ	Time (UTC)	Lat	long	MIPAS Orbit	Time (UTC)	Lat	Long
3 Jan 2010	sr34426	13:22:21	54.78	−72.91	41018	15:10:28	54.71	−72.95
4 Feb 2010	sr34898	13:53:50	67.27	−71.25	41476	15:01:10	67.19	−70.93
25 May 2010	sr36514	04:27:21	68.86	−59.05	43043	02:06:49	68.60	−59.45
10 Jul 2010	sr37203	23:03:33	−59.27	−211.3	43714	23:56:31	−59.16	−210.87

ACPD
14, 18127–18180, 2014

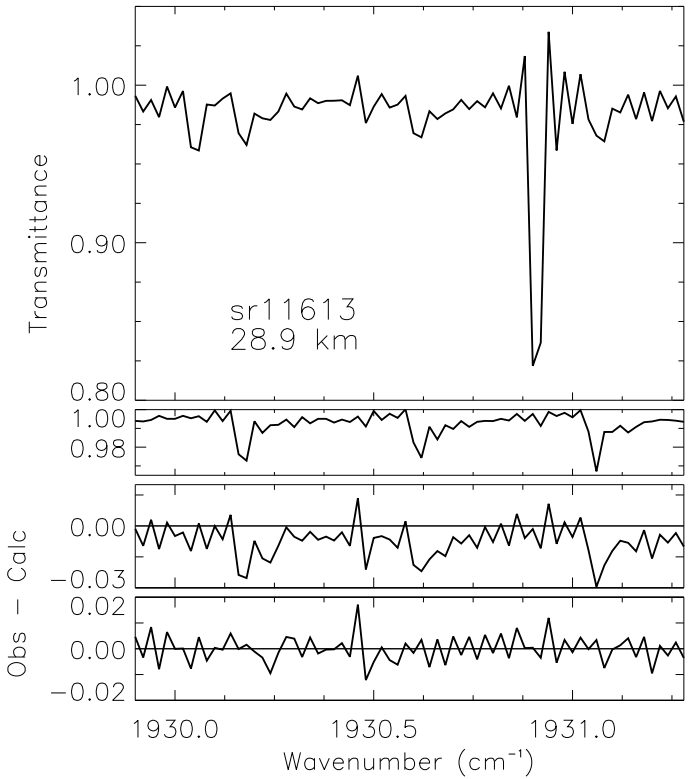

Figure 1. Top panel: an ACE-FTS transmittance spectrum covering the 1929.9–131.3 cm^{-1} microwindow for occultation ss11613 (recorded on 9 October 2005 south of Mexico, over the Pacific Ocean) at a tangent height of 28.9 km. Second panel: the calculated COF_2 transmittance contribution to the measurement (~ 3 %). Third panel: the observed – calculated residuals for the retrieval without the inclusion of COF_2 in the forward model. Bottom panel: the total observed – calculated residuals for the retrieval.

ACPD
14, 18127–18180, 2014

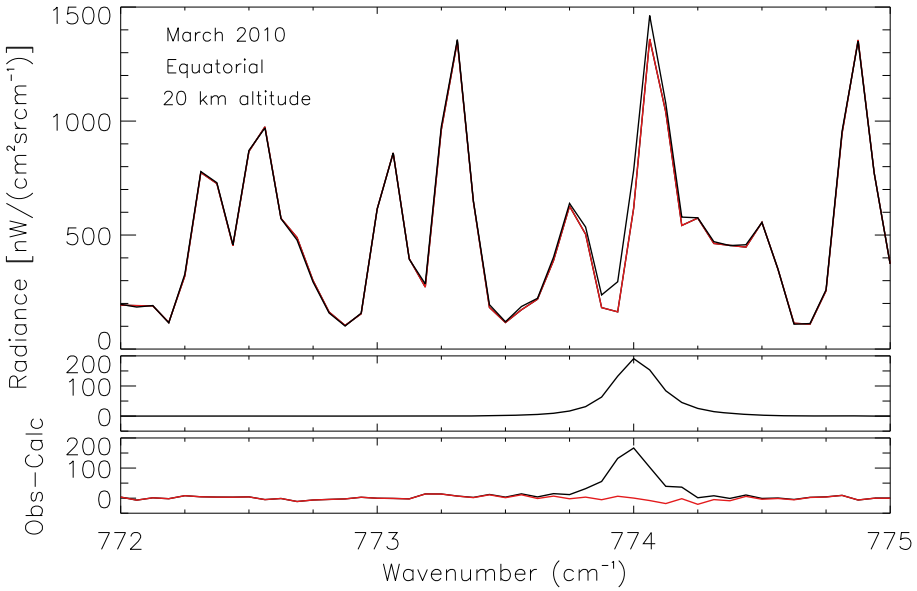

Figure 2. Top panel: an averaged MIPAS radiance spectrum (in black) for equatorial measurements taken in March 2010 covering the 772–775 cm^{-1} microwindow and interpolated to 20 km altitude; in red is the averaged calculated spectrum without the inclusion of COF_2 in the forward model. Second panel: the calculated COF_2 contribution to the spectrum. Bottom panel: the observed – calculated residuals for the retrieval, with and without COF_2 included in the forward model (in red and black, respectively).

ACPD
14, 18127–18180, 2014

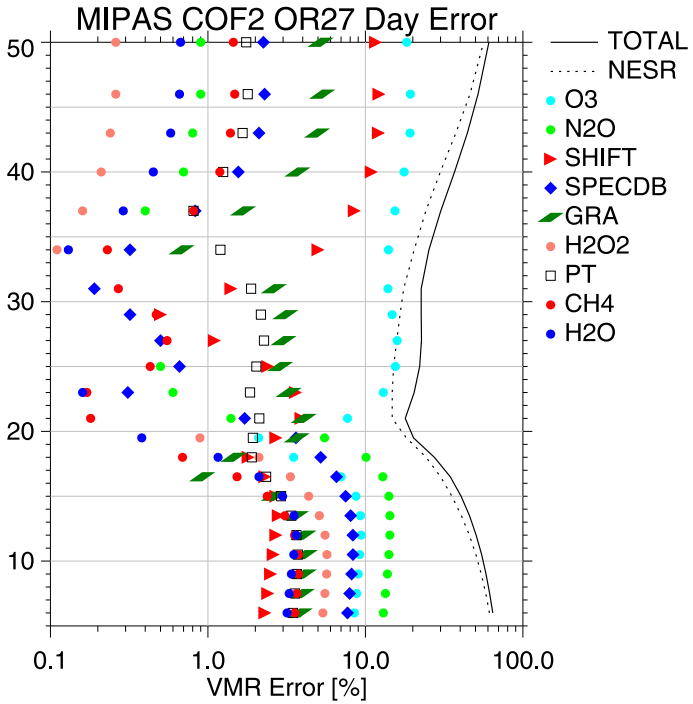

Figure 3. The single-profile total error budget for the MIPAS COF_2 retrieval. The total error is computed by propagating a number of independent error sources expressed as spectra through the retrieval gain matrix, including both spectral correlations and correlations through the pressure-temperature (PT) retrieval. Note that NESR is the noise equivalent spectral radiance, SHIFT refers to the uncertainty in the spectral calibration ($\pm 0.001\,cm^{-1}$), SPECDB (spectroscopic database errors) refers to uncertainties in the strength, position and width of COF_2 infrared lines, and GRA refers to the uncertainty due to an assumed ±1 K/100 km horizontal temperature gradient. More details are contained in the text. Total errors are typically 20–30 % between 20–40 km.

ACPD
14, 18127–18180, 2014

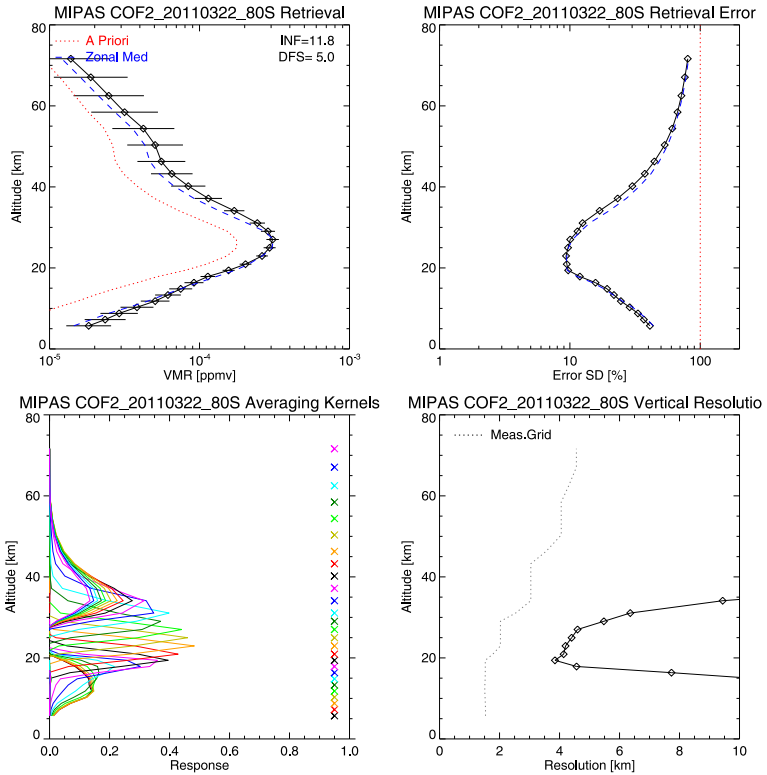

Figure 4. Top left: retrieved MIPAS COF_2 profile at 80° S latitude from 22 March 2011, its corresponding a priori profile, and the median of all the profiles that day within 5° latitude. Top right: the corresponding random error for the profile, ∼ 10 % at the profile peak. Bottom left: the averaging kernel rows for the retrieval, with crosses on the right axis marking the perturbation height for each row. Bottom right: the vertical resolution of the MIPAs retrieval is ∼ 4–6 km near the profile peak, dropping off outside this range.

ACPD
14, 18127–18180, 2014

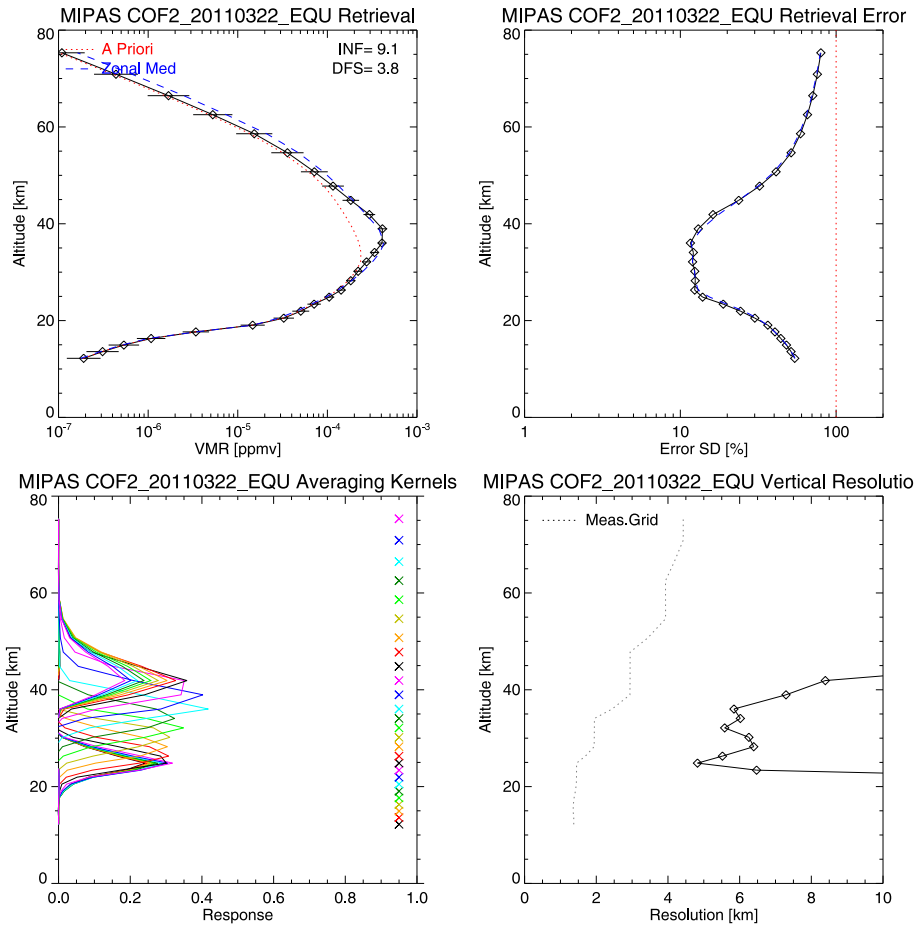

Figure 5. As in Fig. 4, but for MIPAS COF_2 profile at 0° latitude from 22 March 2011.

ACPD
14, 18127–18180, 2014

Satellite observations of stratospheric carbonyl fluoride

J. J. Harrison et al.

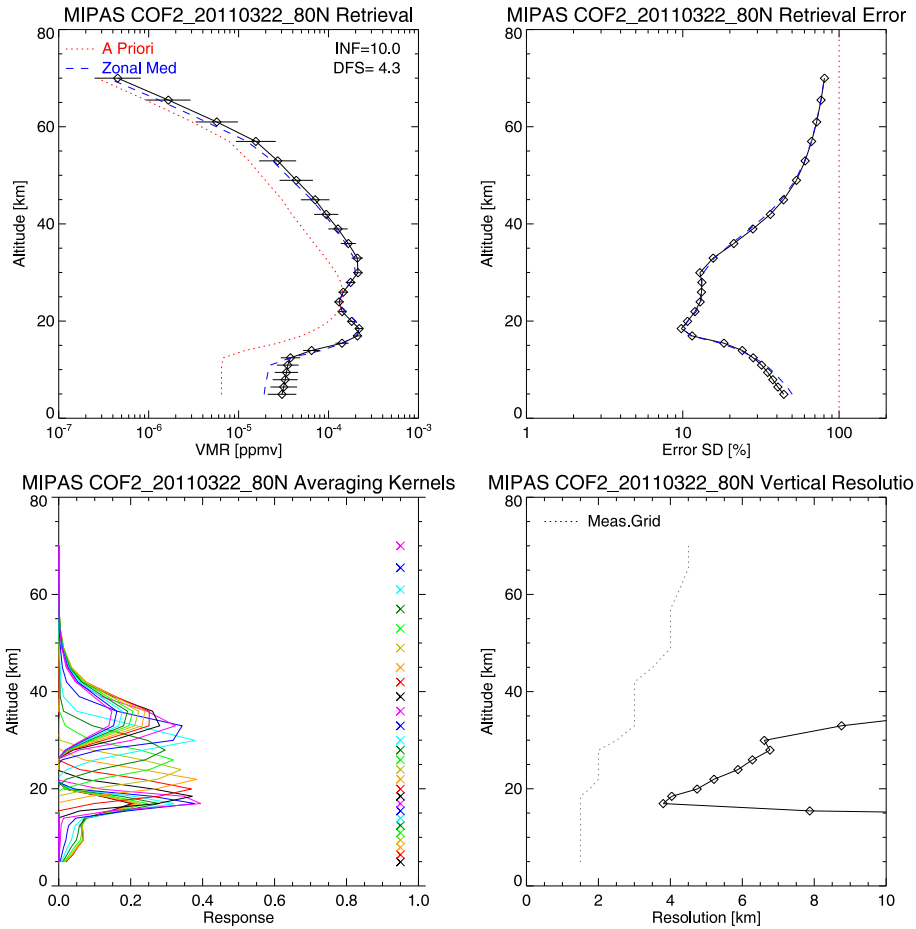

Figure 6. As in Fig. 4, but for MIPAS COF_2 profile at 80° N latitude from 22 March 2011.

ACPD
14, 18127–18180, 2014

Satellite observations of stratospheric carbonyl fluoride

J. J. Harrison et al.

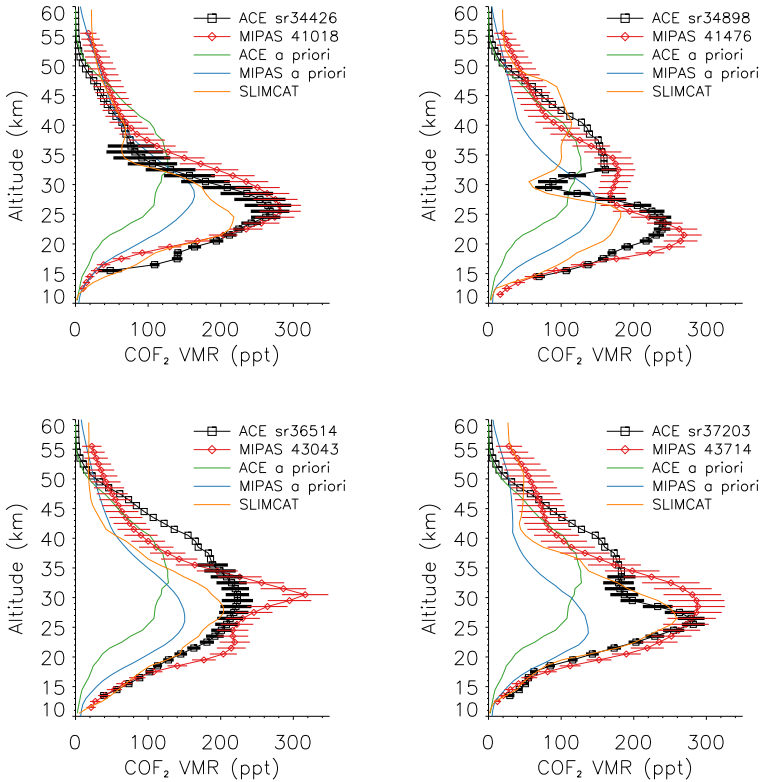

Figure 7. ACE-FTS and MIPAS near-coincident individual profiles taken from the period September 2009 to August 2010. The locations and times of the eight observations can be found in Table 6. The plots also contain the a priori profiles, and calculated SLIMCAT profiles for the location and time of each ACE-FTS observation.

ACPD
14, 18127–18180, 2014

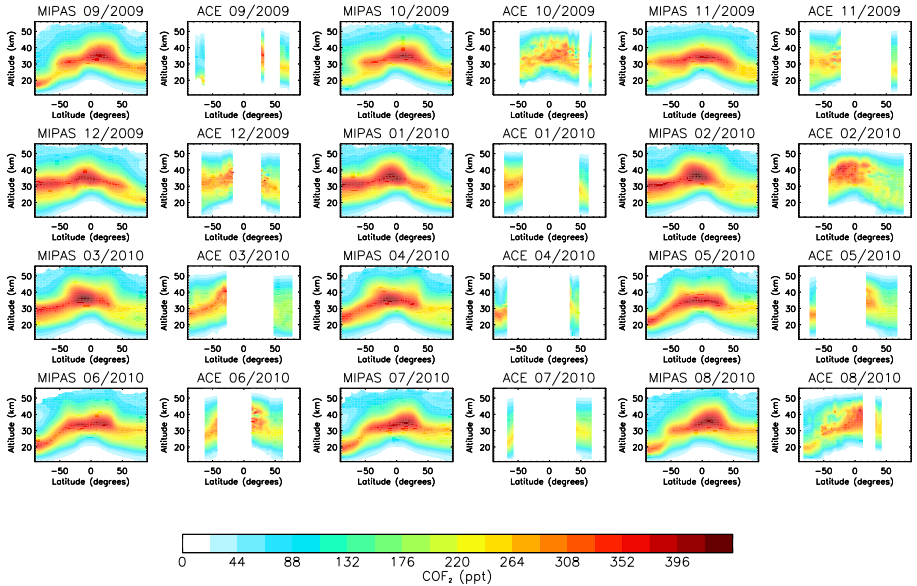

Figure 8. MIPAS and ACE zonal means between September 2009 and August 2010. The plotted VMRs are the averages for each month of all filtered data at each altitude within 5° latitude bins. Note that the global coverage of the ACE-FTS observations between September 2009 and August 2010 is poorer and noisier in appearance than MIPAS, particularly in the tropics. A full discussion of the seasonal variation in the COF_2 distribution is provided in the text.

ACPD
14, 18127–18180, 2014

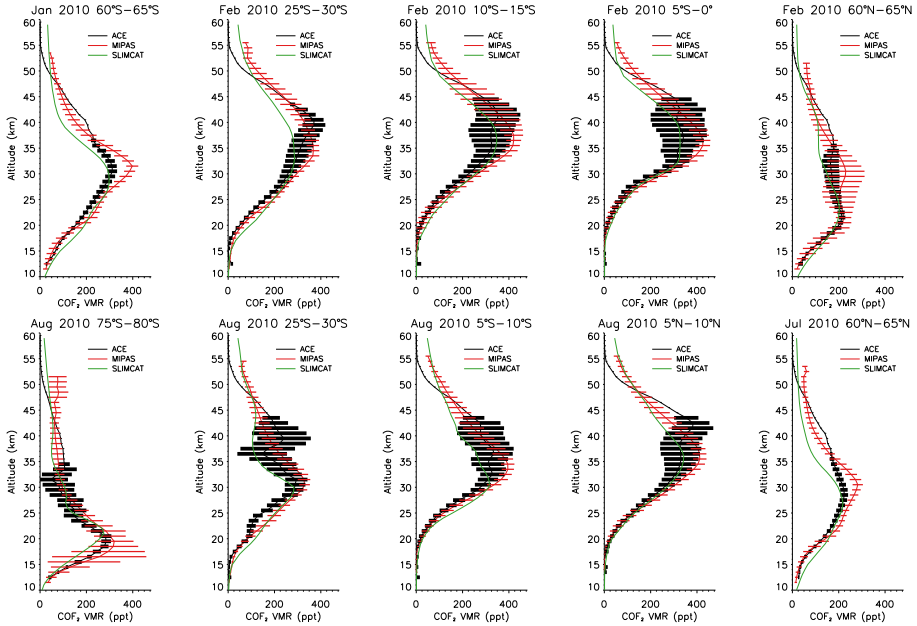

Figure 9. A representative set of MIPAS and ACE individual latitude bins, with errors, taken from Fig. 8. SLIMCAT calculations are also included. A full discussion of the inter-comparison is provided in the text.

ACPD
14, 18127–18180, 2014

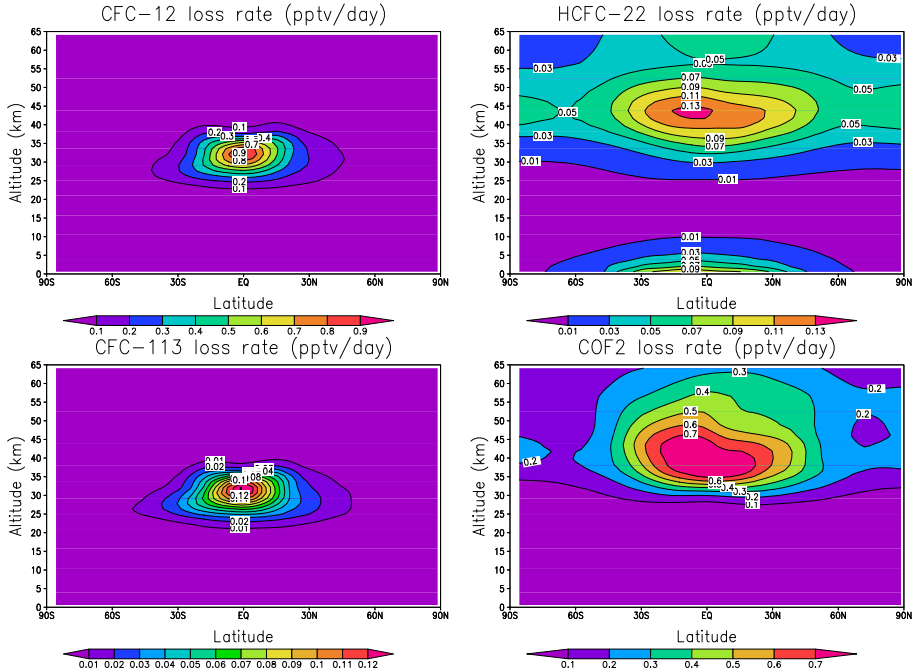

Figure 10. Average loss rates (annual mean zonal mean; pptv day^{-1}) calculated by SLIMCAT for COF_2 and its three main source gases, CFC-12, HCFC-22, and CFC-113. Full details of the loss mechanisms are provided in the text.

ACPD
14, 18127–18180, 2014

Satellite observations of stratospheric carbonyl fluoride

J. J. Harrison et al.

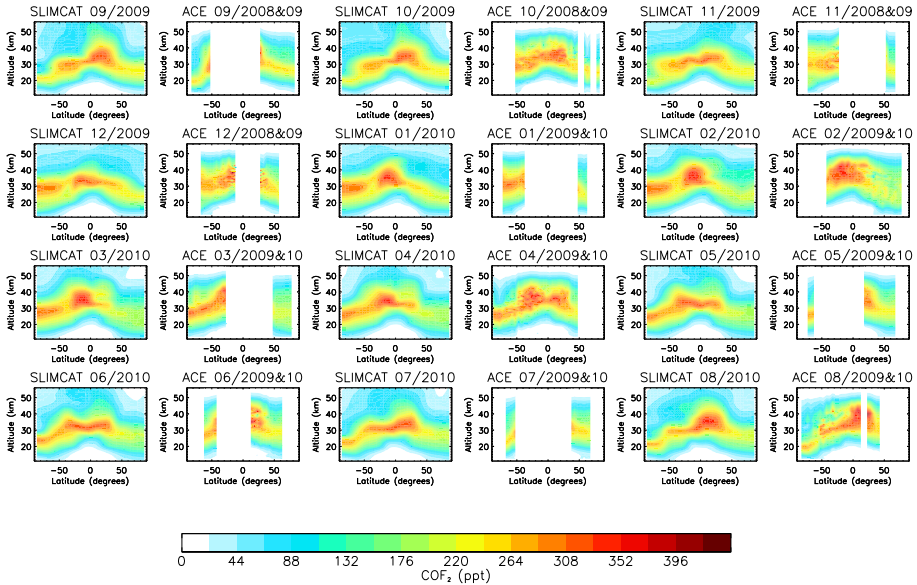

Figure 11. A comparison between monthly SLIMCAT and ACE zonal means (September 2009 to August 2010). In order to reduce the noise and increase the latitude coverage for the comparison, the plotted ACE data have been extended to the previous year. A full discussion of the seasonal variation in the COF_2 distribution is provided in the text.

ACPD
14, 18127–18180, 2014

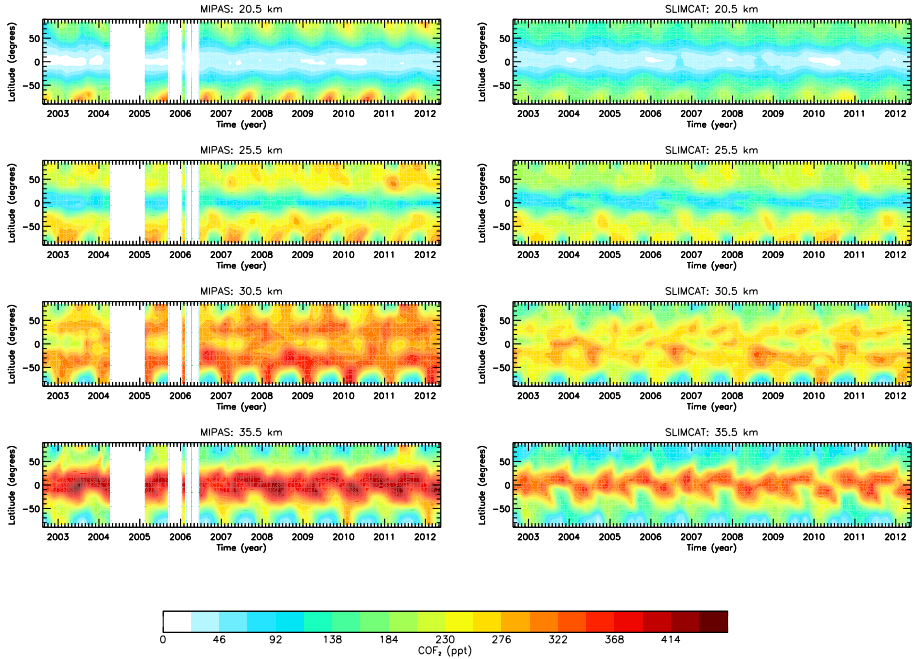

Figure 12. The MIPAS and SLIMCAT COF_2 time series between July 2002 and April 2012 for all latitudes at selected altitudes.

ACPD
14, 18127–18180, 2014

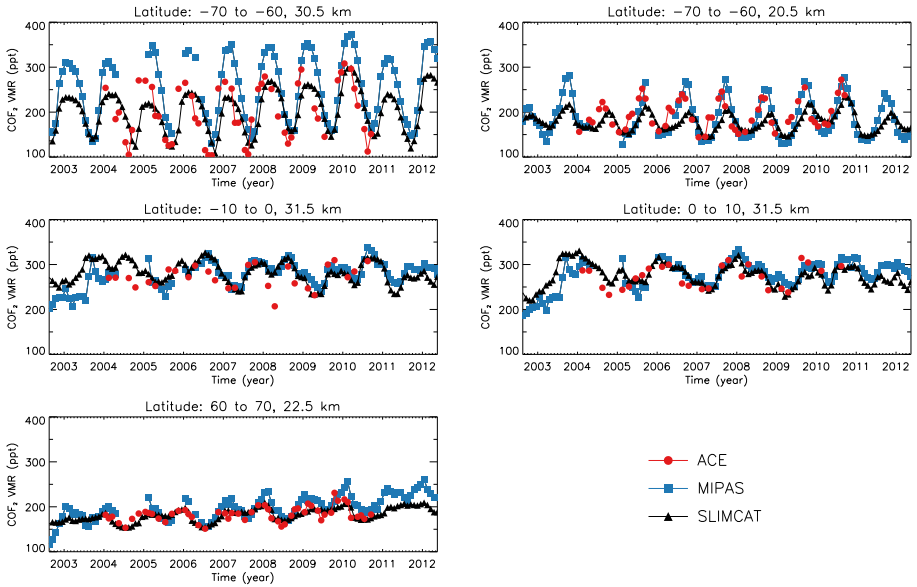

Figure 13. The ACE, MIPAS and SLIMCAT COF_2 time series between July 2002 and April 2012 for five altitude–latitude bin combinations.

ACPD
14, 18127–18180, 2014

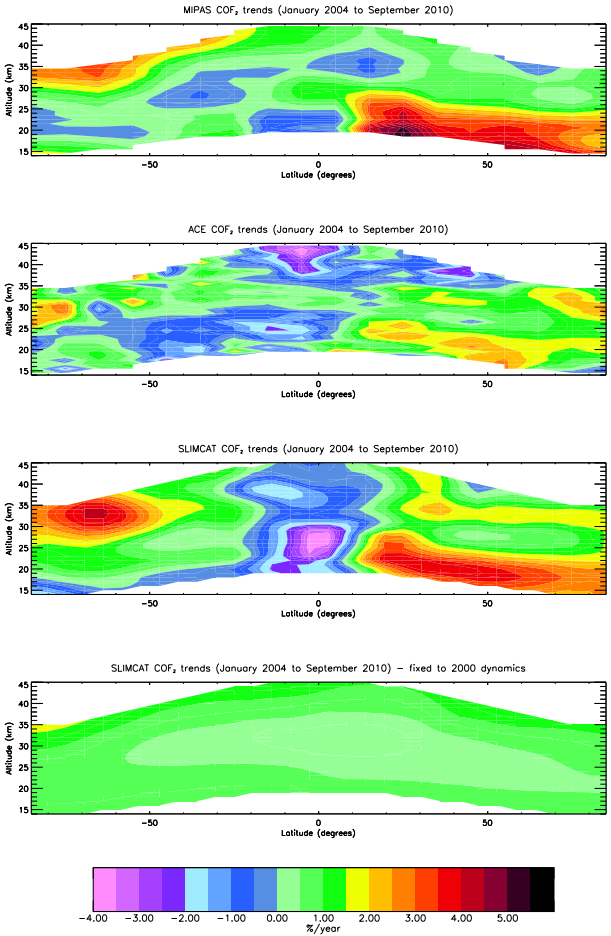

Figure 14. Annual percentage trends (January 2004 to September 2010) for ACE, MIPAS, and SLIMCAT as a function of latitude and altitude. A full discussion of these trends is provided in the text.

ACPD
14, 18127–18180, 2014

Satellite observations of stratospheric carbonyl fluoride

J. J. Harrison et al.